WHU-SGCC: A novel approach for blending daily satellite (CHIRP) and precipitation observations over the Jinsha River Basin

Gaoyun Shen[1], Nengcheng Chen[1,2], Wei Wang[1,2], Zeqiang Chen [1,2]

[1] State Key Laboratory of Information Engineering in Surveying, Mapping and Remote Sensing, Wuhan University, 129 Luoyu Road, Wuhan 430079, China

[2] Collaborative Innovation Center of Geospatial Technology, Wuhan 430079, China

Correspondence to: ZeqiangChen@whu.edu.cn; Tel.: +86 13871025965; Fax: +86 27 68778229.

Abstract. Accurate and consistent satellite-based precipitation estimates blended with rain gauge data are important for regional precipitation monitoring and hydrological applications, especially in regions with limited rain gauges. However, the existing fusion precipitation estimates often have large uncertainties over mountainous areas with complex topography and sparse rain gauges, and most of the existing data blending algorithms are not good at removing the day-by-day errors. Therefore, the development of effective methods for high-accuracy precipitation estimates over complex terrain and at a daily scale is of vital importance for mountainous hydrological applications. This study aims to offer a novel approach for blending daily precipitation gauge data and the Climate Hazards Group Infrared Precipitation (CHIRP; daily, 0.05°) satellite-derived precipitation developed by UC Santa Barbara over the Jinsha River Basin from 1994 to 2014. This method is called the Wuhan University Satellite and Gauge precipitation Collaborated Correction (WHU-SGCC). The results show that the WHU-SGCC method is effective for liquid precipitation error adjustments from points to surfaces as evaluated by multiple error statistics and from different perspectives. Compared with CHIRP and CHIRP with station data (CHIRPS), the precipitation adjusted by the WHU-SGCC method has greater accuracy, with overall average improvements of the Pearson's correlation coefficient (PCC) by 0.01-0.23 and 0.06-0.32, respectively, and decreases in the root mean square error (RMSE) by 0.06–0.1 mm and 0.2-3 mm, respectively. In addition, the NSE of the WHU-SGCC provides substantial improvements than CHIRP and CHIRPS, which reached 0.2836, 0.2944 and 0.1853 in the spring, fall and winter. Daily accuracy evaluations indicate that the WHU-SGCC method has the best ability to reduce precipitation error, with average reductions of 15% and 34% compared to CHIRP and CHIRPS, respectively. Moreover, the accuracy of the spatial distribution of the precipitation estimates derived from the WHU-SGCC method is related to the complexity of the topography. The validation also verifies that the proposed approach is effective at detecting major precipitation events within the Jinsha River Basin. In spite of the correction, the uncertainties in the seasonal precipitation forecasts in the summer and winter are still large, which may due to the homogenization attenuating the simulation of extreme rain event. However, the WHU-SGCC approach may serve as a promising tool to monitor daily precipitation over the Jinsha River Basin, which contains complicated mountainous terrain with sparse rain gauge data, based on the spatial correlation and the historical precipitation characteristics. The daily precipitation estimations at the 0.05° resolution over the Jinsha River Basin during all four seasons from 1990 to 2014, derived from WHU-SGCC are available at the PANGAEA Data Publisher for Earth & Environmental Science portal (https://doi.pangaea.de/10.1594/PANGAEA.900620).

1 Introduction

Accurate and consistent estimates of precipitation are vital for hydrological modelling, flood forecasting and climatological studies in support of better planning and decision making (Agutu et al., 2017;Cattani et al., 2018;Roy et al., 2017). In general, ground-based gauge networks include a substantial number of liquid precipitation observations measured with high accuracy, high temporal resolution, and long historical records. However, the sparse distribution and point measurements limit the accurate estimation of spatially gridded rainfall (Martens et al., 2013).

Due to the sparseness and uneven spatial distribution of rain gauges and the high proportion of missing data, satellite-derived

precipitation data are an attractive supplement offering the advantage of plentiful information with high spatio-temporal resolution over widespread regions, particularly over oceans, high elevation mountainous regions, and other remote regions where gauge networks are difficult to deploy. However, satellite estimates are susceptible to systematic biases that can influence hydrological modelling and the retrieval algorithms are relatively insensitive to light rainfall events, especially in complex terrain, resulting in underestimations of the magnitudes of precipitation events (Behrangi et al., 2014;Thiemig et al., 2013;Yang et al., 2017). Without adjustments, inaccurate satellite-based precipitation estimates will lead to unreliable assessments of risk and reliability (AghaKouchak et al., 2011).

Accordingly, many kinds of precipitation estimates combining multiple sources and datasets are available. Table 1 shows the temporal and spatial resolution of current major satellite-based precipitation datasets. Since 1997, the Tropical Rainfall Measurement Mission (TRMM) has improved satellite-based rainfall retrievals over tropical regions (Kummerow et al., 1998;Simpson et al., 1988). High spatial and temporal resolution multi-satellite precipitation products have been developed continuously during the TRMM era (Maggioni et al., 2016), including: (1) the TRMM Multisatellite Precipitation Analysis (TMPA) products, which are derived from gauge-satellite fusing (Huffman et al., 2010;Vila et al., 2009); (2) the Climate Prediction Center (CPC) morphing technique (Joyce et al., 2004;Joyce and Xie, 2011;Xie et al., 2017), which integrates geosynchronous infrared (GEO IR) and polar-orbiting microwave (PMW) sensor data and is available three-hourly on a grid with a spacing of 0.25°; (3) the Precipitation Estimation from Remotely Sensed Information using Artificial Neural Networks - Climate Data Record (PERSIANN-CDR) produced by the PERSIANN algorithm, which has daily temporal and $0.25° \times 0.25°$ spatial resolutions (Ashouri et al., 2015); and (4) the Global Satellite Mapping of Precipitation (GSMaP) project, which produces global rainfall estimates in near–real time and applies the motion vector Kalman filter based on physical models (GSMaP-NRT and GSMaP-MVK, respectively) (Aonashi et al., 2009;Ushio et al., 2009;Ushio and Kachi, 2010). In 2014, the Global Precipitation Measurement (GPM) satellite was launched after the success of the TRMM satellite by a cooperation between the National Aeronautics and Space Administration (NASA) and Japan Aerospace Exploration Agency (JAXA) (Mahmoud et al., 2018;Ning et al., 2016). The main core observatory satellite (GPM) integrates advanced radar and radiometer systems to obtain the precipitation physics and takes advantages of TMPA, the Climate Prediction Center morphing technique (CMORPH), and PERSIANN algorithms to offer high spatiotemporal resolution products ($0.1° \times 0.1°$, half-hourly) of global real-time precipitation estimates (Huffman et al., 2018; Skofronick-Jackson et al., 2017; Hou et al., 2014). Nevertheless, the major aforementioned products have only been available since 1998, which limits long-term climatological studies. Only the PERSIANN-CDR data set has temporal coverage since 1983. However, the spatial resolution of PERSIANN-CDR is relatively coarse, and the data resolution must be degraded to achieve high accuracy in precipitation monitoring. To fill the gap in high resolution and long-term global multi-satellite precipitation monitoring, the Multi-Source Weighted-Ensemble Precipitation (MSWEP) product (Beck et al., 2017; Beck et al., 2019), and the Climate Hazards Group Infrared Precipitation with Station data (CHIRPS) product from UC Santa Barbara (Funk et al., 2015 a) were developed. MSWEP is a precipitation data set with global coverage available at 0.1° spatial resolution and at three-hourly, daily, and monthly temporal resolutions. MSWEP is multi-source data that takes advantage of the complementary strengths of gauge-, satellite-, and reanalysis-based data. However, to provide precipitation estimates at a higher spatial resolution, the CHIRPS data set is used in this study.

CHIRPS is a longer length precipitation data series with a higher spatial resolution (0.05°) that, merges three types of information: global climatology, satellite estimates and in situ observations. The CHIRPS precipitation dataset with several temporal and spatial scales has been evaluated in Brazil (Nogueira et al., 2018;Paredes-Trejo et al., 2017), Chile (Yang et al., 2016;Zambrano-Bigiarini et al., 2017), China (Bai et al., 2018), Cyprus (Katsanos et al., 2016a;Katsanos et al., 2016b), India (Ali and Mishra, 2017; Prakash, 2019) and Italy (Duan et al., 2016). However, the temporal resolutions of these applications were mainly at seasonal and monthly scales, lacking the evaluation and correction of daily precipitation. Additionally, despite

the great potential of gauge-satellite fusing products for large-scale environmental monitoring, there are still large discrepancies with ground observations at the sub-regional level where these data have been applied. Furthermore, the CHIRPS product's reliability has not been analysed in detail over the Jinsha River Basin in China, particularly at a daily scale. The Jinsha River Basin is a typical study area with complex and varied terrain, an uneven spatial distribution of precipitation, and a sparse spatial distribution of rain gauges, which limit high accuracy precipitation monitoring. The existing research indicates that estimations over mountainous areas with complex topography often have large uncertainties and errors due to the topography, seasonality, climate impact and sparseness of rain gauges (Derin et al., 2016;Maggioni and Massari, 2018;Zambrano-Bigiarini et al., 2017). Moreover, Bai et al. (2018) evaluates CHIRPS over mainland China and indicates that the performance of CHIRPS is poor over the Sichuan Basin and the Northern China Plain, which have complex terrain with substantial variations in elevation. Additionally, Trejo et al. (2016) shows that CHIRPS overestimates low monthly rainfall and underestimates high monthly rainfall using several numerical metrics and that the rainfall event frequency is overestimated outside the rainy season.

Table 1 Coverage and spatiotemporal resolutions of major satellite precipitation datasets.

Product	Temporal resolution	Spatial resolution	Period	Coverage
TRMM 3B42-RT	3 hourly	0.25°	1998-present	50°S-50°N
CMORPH	30 min	8 km	1998-	60°S-60°N
PERSIANN-CDR	Daily	0.25°	1983-(delayed) present	60°S-60°N
GsMaP-NRT	hourly	0.01°	2007	60°S-60°N
GsMaP-MVK	hourly	0.01°	2000	60°S-60°N
GPM	30 min/Hourly/ 3 hourly/Daily/3Day/7 Day/Monthly	0.1°/0.25°/0.05°/5°	2014-present	60°S-60°N 70°N-70°S 90°N-90°S
MSWEP	3 hourly/Daily/Monthly	0.1°	1979-2017	90°N-90°S
CHIRPS	Annual/Monthly/ Dekad/Pentad/Daily	0.05°/0.25°	1981- present	50°S-50°N

To overcome these limitations, many studies have focused on proposing effective methodologies for blending rain gauge observations, satellite-based precipitation estimates, and sometimes radar data to take advantage of each dataset. Many numerical models have been established with these datasets for high-accuracy precipitation estimations, such as bias adjustment by a quantile mapping (QM) approach (Yang et al., 2016), Bayesian kriging (BK) (Verdin et al., 2015) and a conditional merging technique (Berndt et al., 2014). The QM approach is a distribution-based approach, which works with historical data for bias adjustment and is effective at reducing the systematic bias of regional climate model precipitation estimates at monthly or seasonal scales (Chen et al., 2013). However, the QM approach offers very limited improvement in removing day-by-day errors. The BK approach provides very good model fit with precipitation observations, but the Gaussian assumption of the BK model is invalid for daily scales. Overall, there is a lack of effective methods for high-accuracy precipitation estimates over complex terrain at a daily scale.

As such, due to the poor performance at the sub-regional scale, the gauge-satellite fusing algorithms can be assumed to limit high accuracy estimations in the process of CHIRPS data production. Therefore, the aim of this article is to present a novel approach for reblending daily liquid precipitation gauge data and the Climate Hazards Group Infrared Precipitation (CHIRP) satellite-derived precipitation estimates developed by UC Santa Barbara, over the Jinsha River Basin. We use precipitation to denote liquid precipitation throughout the text. The CHIRP data are the raw data of CHIRPS before blending with the rain gauge data. The objective is to build corresponding precipitation models that consider terrain factors and precipitation characteristics to produce high-quality precipitation estimates. This novel method is called the Wuhan University Satellite and Gauge precipitation Collaborated Correction (WHU-SGCC) method. We demonstrate this method by applying it to daily precipitation over the Jinsha River Basin in the different seasons from 1990 to 2014. The results support the validity of the proposed approach for producing refined satellite-gauge precipitation estimates over mountainous areas.

The remainder of this paper is organized as follows: Section 2 describes the study region, rain gauges and CHIRPS dataset used in this study. Section 3 presents the principle of the WHU-SGCC approach for high-accuracy daily precipitation estimates.

117 The results and discussion are analysed in Section 4, the data available are described in Section 5, and the conclusions and
118 future work are presented in Section 6.

119 **2 Study Region and Data**

120 **2.1 Study Region**

121 The Yangtze River, one of the largest and most important rivers in Southeast Asia, originates on the Tibetan Plateau and extends
122 approximately 6300 km eastward to the East China Sea. The river's catchment covers an area of approximately ~180×10^4
123 km^2 and the average annual precipitation is approximately 1100 mm (Zhang et al., 2019).The Yangtze River is divided into
124 nine sub-basins, the upper drainage basin is the Jinsha River Basin, which flows through the provinces of Qinghai, Sichuan,
125 and Yunnan in western China. Within the Jinsha River Basin, the total river length is 3486 km, accounting for 77% of the
126 length of the upper Yangtze River, and covering a watershed area of 460×10^3 km^2. The location of the Jinsha River Basin is
127 shown in Fig. 1, and it covers the eastern part of the Tibetan Plateau and part of the Hengduan Mountains. The southern portion
128 of the river basin is the Northern Yunnan Plateau and the eastern portion includes a wide area of the southwestern margin of
129 the Sichuan Basin. Crossing complex and varied terrains, the elevation of the Jinsha River ranges from 263 to 6575 m above
130 sea level, which results in significant temporal and spatial climate and weather variations inside the basin. The average annual
131 precipitation of the Jinsha River Basin is approximately 710 mm, the average annual precipitation of the lower reaches is
132 approximately 900-1300 mm, and the average annual precipitation of the middle and upper reaches is approximately 600-800
133 mm (Yuan et al., 2018). The Jinsha River Basin has four seasons: spring (March-April-May), summer (June-July-August), fall
134 (September-October-November) and winter (December-January-February). The climate of the Jinsha River Basin is affected
135 by oceanic southwest and southeast monsoons, resulting in more precipitation during the summer. Therefore, the blending of
136 satellite estimations with gauge observations during the different seasons is the main focus of this research.
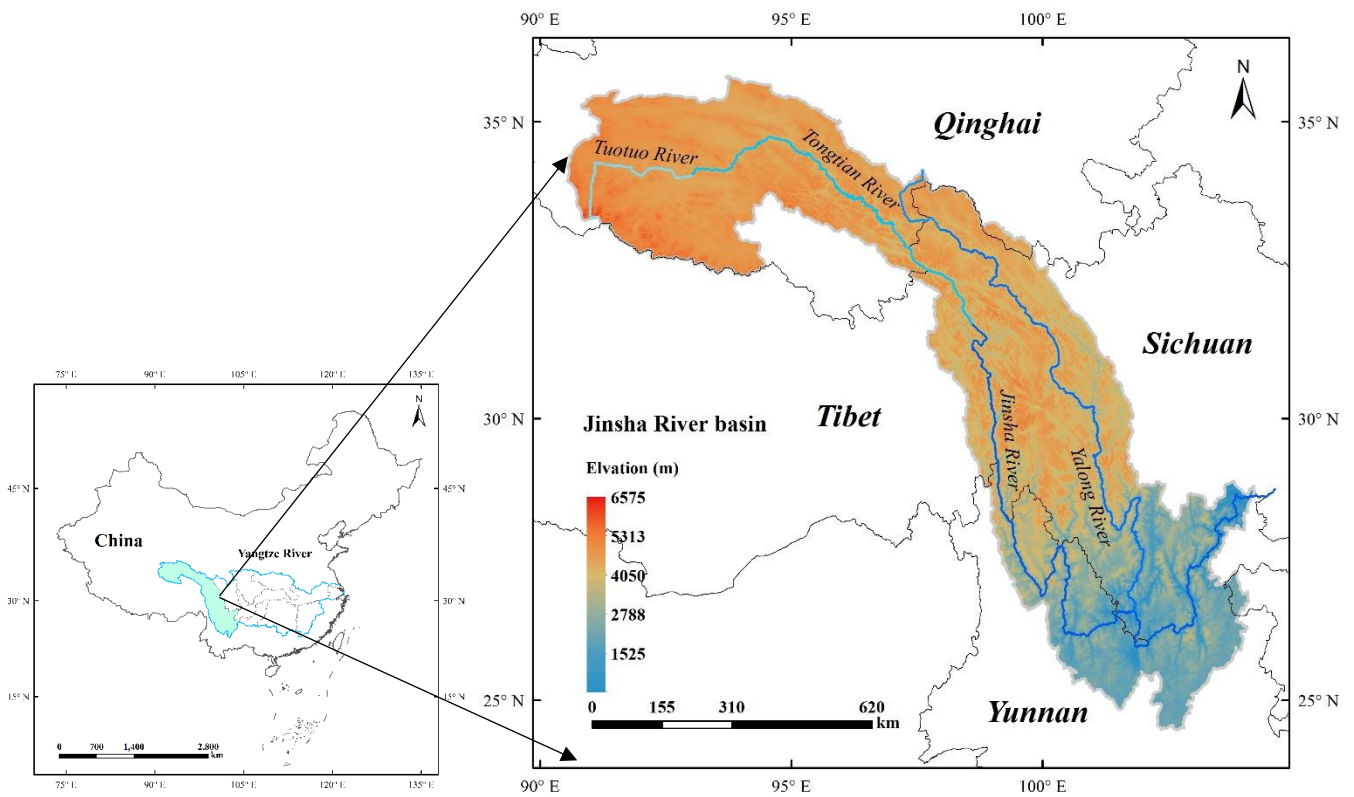
137
138 **Figure 1** Location of the study area with key topographic features.

139 **2.2 Study Data**

2.2.1 Precipitation gauge observations

Daily rain gauge observations at 30 national standard rain stations within the Jinsha River Basin from 1 March 1990 to February 2015 were provided by the National Climate Centre (NCC) of the China Meteorological Administration (CMA) (http://data.cma.cn/data/cdcdetail/dataCode/SURF_CLI_CHN_MUL_DAY_V3.0.html, last access: 10 December, 2018), which imposes strict quality control at the station, provincial and state levels. The station identification numbers and relevant geographical characteristics are shown in Appendix A, and their uneven spatial distribution is shown in Fig. 2. The selected rain gauges are located in Qinghai, Tibet, Sichuan and Yunnan Provinces but are mainly scattered in Sichuan Province, and the northern river basin contains fewer rain gauges than the southern river basin. In this study, the gauge observations were used as the reference data for the error adjustment of satellite precipitation estimations.

The multi-year (1990-2014) average seasonal precipitation over the Jinsha River Basin increases from north to south (Fig. 2). The dynamic and uneven distribution of precipitation is influenced distinctly by the seasonal climate. Most of the precipitation falls in the summer, with the average seasonal precipitation ranging from less than 250 mm to more than 600 mm, while the average seasonal precipitation during the winter is no more than 50 mm. The average seasonal precipitation and spatial distribution in the spring are similar with those in the fall, with values concentrated in the range of 50 mm to 200 mm.

(a) Spring (b) Summer

(c) Fall   (d) Winter
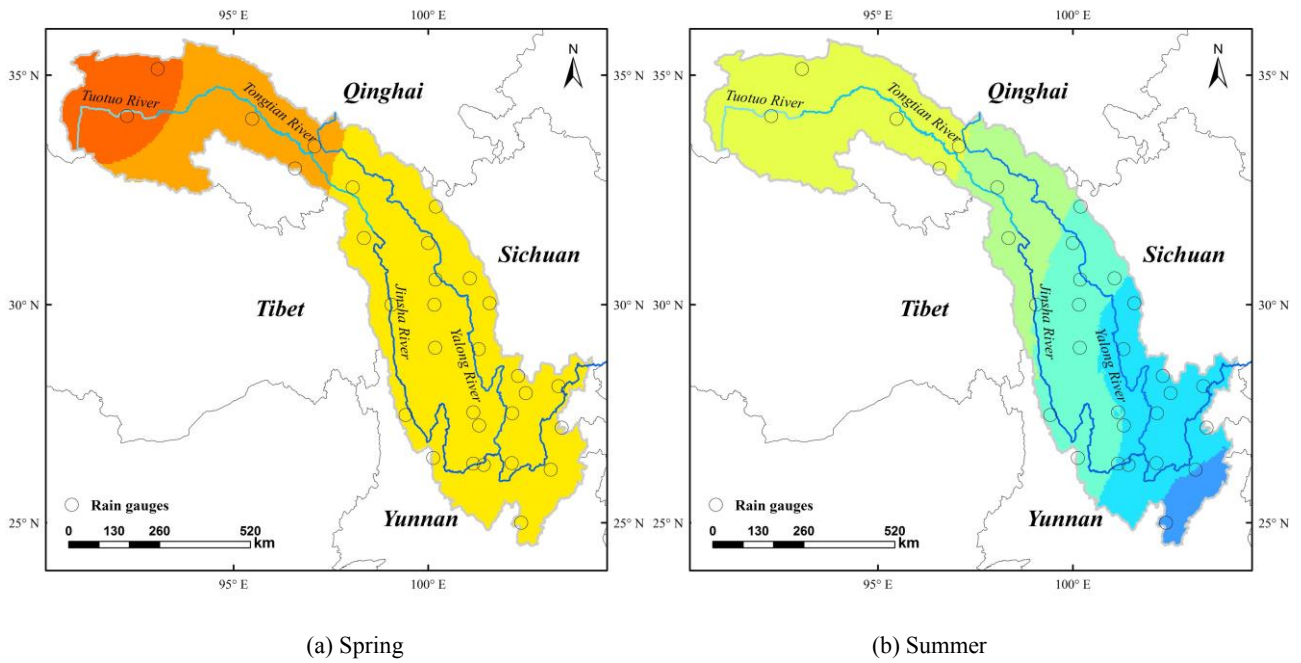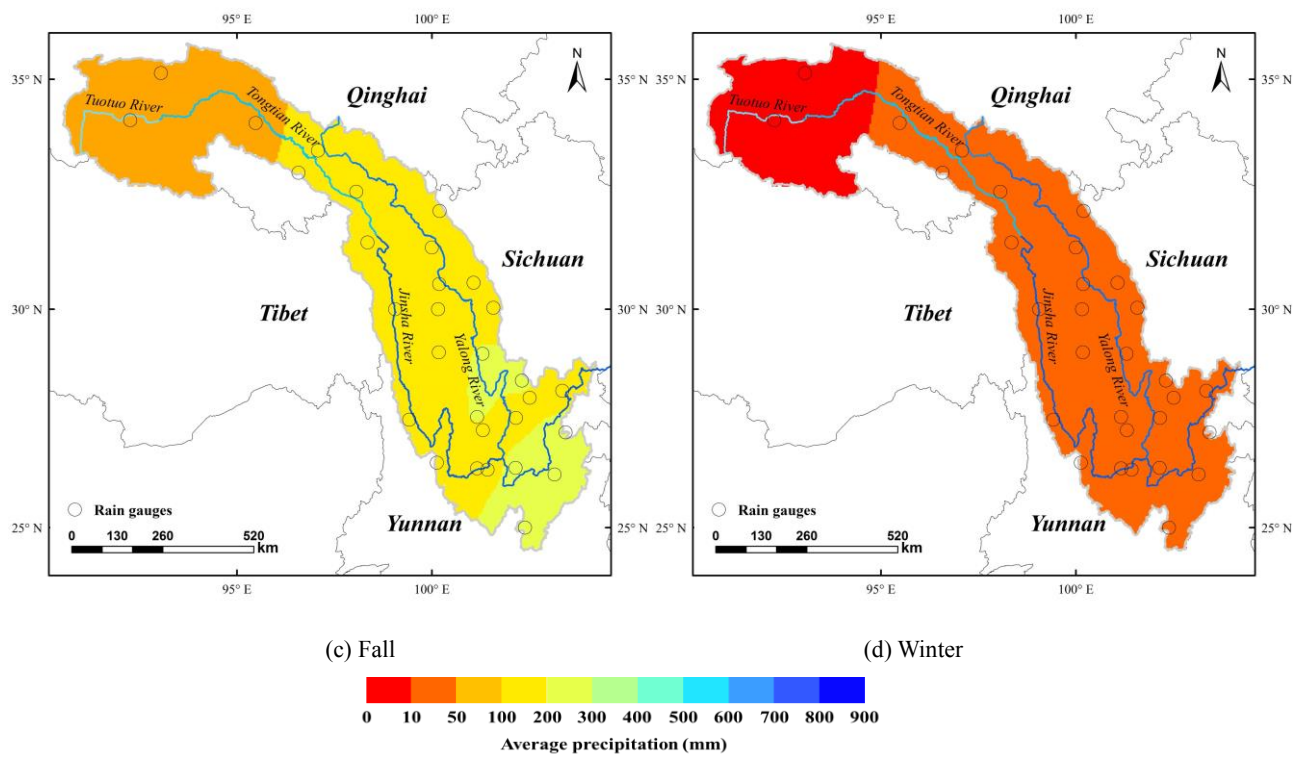
Figure 2 The multi-year (1990-2014) average seasonal precipitation over the Jinsha River Basin interpolated from30 rain gauges downloaded from the China Meteorological Administration stations.

2.2.2 CHIRPS satellite-gauge fusion precipitation estimates

The CHIRPS v.2 dataset, a satellite-based daily rainfall product, is available online at ftp://ftp.chg.ucsb.edu/pub/org/chg/products/CHIRPS-2.0/global_daily/tifs/p05/ (last access: 10 December, 2018). It covers a quasi-global area (land only, 50° S-50° N) a several temporal scales (daily, pentad, dekad, monthly and annual temporal resolutions) and a high spatial resolution (0.05°) (Rivera et al., 2018). This dataset contains a wide variety of satellite-based rainfall products derived from a multiple data sources and incorporates five data types: (1) the monthly precipitation from CHPClim v.1.0 (Climate Hazards Group's Precipitation Climatology version 1) derived from a combination of satellite fields, gridded physiographic indicators, and in situ climate normal with the geospatial modelling approach based on moving window regressions and inverse distance weighting interpolation (Funk et al., 2015 b); (2) quasi-global geostationary thermal infrared (IR) satellite observations; (3)the TRMM 3B42 product (Huffman et al., 2007); (4) the CFS (Climate Forecast System, version 2) atmospheric model rainfall fields from NOAA; and (5) surface-based precipitation observations from various sources including national and regional meteorological services. The differences from other frequently used precipitation products are the higher resolution of 0.05° , wider coverage and longer length data series from 1981 to near-real time (Funk et al., 2015 a).

CHIRPS is the blended product of a two-part process. First, IR precipitation (IRP) pentad rainfall estimates are fused with corresponding CHPClim pentad data to produce an unbiased gridded estimate, called CHIRP, which is available online at ftp://ftp.chg.ucsb.edu/pub/org/chg/products/CHIRP/daily/ (last access: 10 December, 2018). In the second part of the process, the CHIRP data are blended with in situ precipitation observations obtained from a variety of sources, including national and regional meteorological services by means of a modified inverse-distance weighting algorithm to create the final blended product, CHIRPS (Funk et al., 2014). The daily CHIRP satellite-based data over the Jinsha River Basin from 1990.02 to 2015.02 were selected as the input for WHU-SGCC blending with rain observations, and the corresponding daily CHIRPS blended data was used for comparisons of the precipitation accuracy.

The blended in situ daily precipitation observations of the CHIRPS data come from a variety of sources, such as the daily GHCN archive (Durre et al., 2010), the Global Summary of the Day dataset (GSOD) provided by NOAA's National Climatic Data Center, the World Meteorological Organization's Global Telecommunication System (GTS) daily archive provided by

NOAA CPC, and more than a dozen national and regional meteorological services. However, the stations for daily CHIRPS data have a different spatial distribution than those downloaded from the CMA, and the precipitation values used for CHIRPS production are the monthly values available online (ftp://ftp.chg.ucsb.edu/pub/org/chg/products/CHIRPS-2.0/diagnostics/monthly_station_data/). For the daily precipitation adjustments over the Jinsha River Basin, the daily gauge observations from the CMA are blended with the daily CHIRP data due to the unknown spatial distribution and precipitation values of gauge stations used in the process of daily CHIRPS merging.

3 Methods

3.1 The WHU-SGCC approach

In this study, the WHU-SGCC approach is to estimates the precipitation at every pixel by blending satellite estimates and rain gauge observations considering the terrain factors and precipitation characteristics. Due to the significant seasonal difference of precipitation, the WHU-SGCC method was applied in the different seasons. Four steps were used to establish the numerical relationship between the gauge stations and the corresponding satellite pixels and for the interpolation of the remaining pixels. The WHU-SGCC method identifies the geographical locations and topographical features of each pixel and applies the four classification and blending rules. A flowchart of the WHU-SGCC method is shown in Fig. 3. The proposed approach was evaluated over the Jinsha River Basin based on 30 gauge stations and CHIRP satellite-based precipitation estimations in the different seasons from 1990 to 2014. The leave-one-out cross validation step was applied to compute the out-of-sample adjusted error with the gauge stations. The WHU-SGCC algorithm was repeated 30 times, each time leaving one station as the validation station.

The basic description of the WHU-SGCC method is given below, and the details are illustrated separately in later sections:

(1) Classify all regional pixels into four types: C1 (pixels including one gauge station in their area), C2 (pixels statistically similar to C1), C3 (pixels statistically similar to C2) and C4 (remaining pixels).

(2) Analyze the relationships between the precipitation observations and the C1, C2, and C3 pixel types, and interpolate for the C4 pixels. These relationships are described by four rules, which are described below as Rules 1 through 4.

(3) Establish statistical models and screen the target pixels based on the four rules.

(4) Correct all of the precipitation pixels in the daily regional precipitation images.
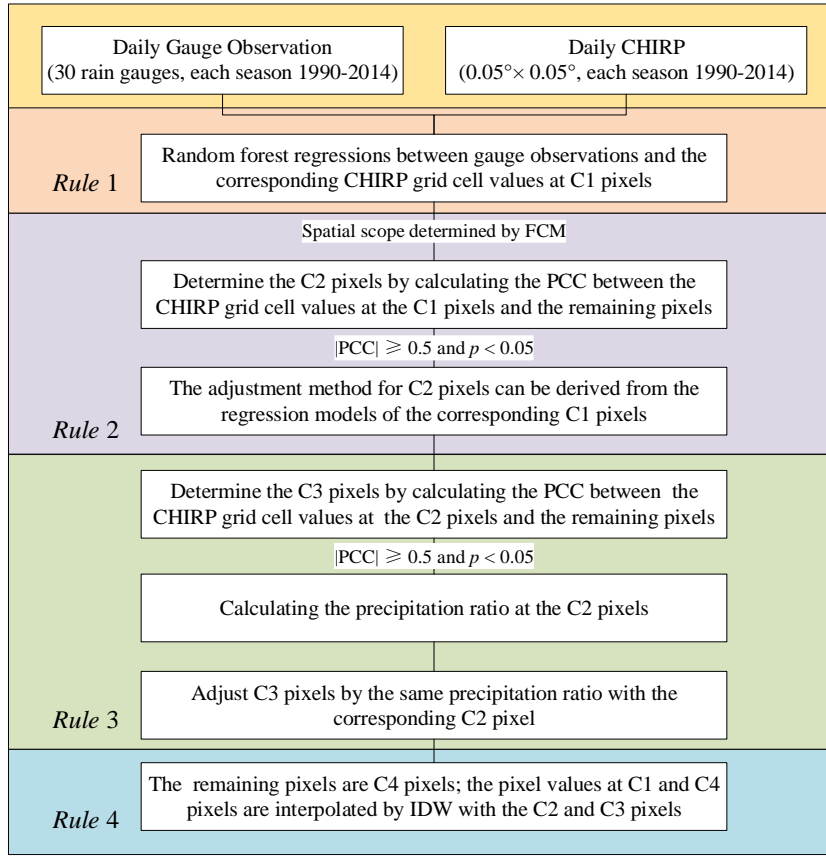
212 **Figure 3** Flowchart of the WHU-SGCC approach with the four rules applied in this study.

213 **3.1.1 Assumptions**

214 (1) Gauge observations are the most accurate, or "true", values for reference purposes. However, the sparseness of the

215 gauges, their uneven spatial distribution, and the high proportion of missing data may limit high accuracy estimation in rainfall

216 monitoring.

217 (2) No major terrain changes occurred during the twenty years (Appendix B).

218 (3) There are no long-held outliers at one pixel in the CHIRP dataset, so Pearson's Correlation Coefficient (PCC) can

219 represent the statistical similarity of the rainfall characteristics among the pixels in a certain spatial area at a seasonal scale.

220 **3.1.2 Rule 1 of the WHU-SGCC method**

221 In general, the satellite precipitation estimations deviated from the ground-based measurements, which were assumed to be

222 the true values. Rule 1 aims to establish a regression model between the historical observations at each gauge and the

223 corresponding CHIRP grid cell values. The regression relationship was derived by random forest regression (RFR) at each

224 gauge station. RFR is a machine-learning algorithm for a predictive model with a large set of regression trees in which each

225 tree in the ensemble is grown from a bootstrap sample (Johnson, 1998) drawn with a replacement from the training set. In the

226 process of establishing regression trees, a subset of variables for each node is selected to avoid overfitting. The final prediction

227 is obtained by combining the results of the prediction methods applied to each bootstrap sample (Genuer et al., 2017). The

228 predicted value is calculated by the average of the values from all of the decision trees. Each tree can be expressed as

229
$$Tree_k = f_{RFR}(Y_o, \Theta_{Y_{s_k}}), \quad k=1\ldots n \tag{1}$$

230 where Y_o denotes the historical observations at each gauge at the C1 pixels, Θ_{Y_s} is a randomly selected vector from Y_s,

231 Y_s denotes the corresponding CHIRP grid cell values at the C1 pixels, n is the number of trees, and f_{RFR} is constructed

232 from the time series Y_o (dependent variable) and Y_s (independent variable) by means of RFR. The bootstrap sample will

233 be the training set used for growing the tree. The error rate (out-of-bag, OOB) left out of one-third of the training data is also

234 monitored to determine the number of decision trees. In this study, the minimum OOB error rate was reached when the

235 number of decision trees n was less than 500 (Appendix C).

236   Rule 1 builds the statistical relationships between the gauge observations and the corresponding CHIRP grid cell values,

237 which is the key idea in correcting the satellite-based precipitation estimations in the entire study area. Because there are 30

238 gauge stations in the study area, 30 regression relationships at the C1 pixels were derived from Rule 1. The values of the C1

239 pixels are not corrected in Rule 1 but are interpolated in Rule 4.

240 **3.1.3 Rule 2 of the WHU-SGCC method**

241 It is reasonable to assume that some pixels are statistically similar to the historical precipitation characteristics of the C1 pixels

242 within a certain area. Therefore, it is feasible to adjust the satellite estimation bias of the C2 pixels by referring to the

243 appropriate regression relationships at the corresponding C1 pixels based on Rule 1.

244   First, the spatial area in which pixels may have highly similar characteristics is established. Several studies indicate that the

245 geographical location, elevation and other terrain information influence the spatial distribution of rainfall, especially in

246 mountainous areas with complex topography (Anders et al., 2006;Long and Singh, 2013). The size of the spatial range is an

247 important parameter to distinguish the spatial similarity and heterogeneity. In the WHU-SGCC method, the fuzzy c-means

248 (FCM) clustering approach was used to determine the spatial range considered for each pixel's terrain factors, including

249 longitude, latitude, elevation, slope, aspect and curvature. The FCM method was developed by J.C. Dunn in 1973 (Dunn,

250 1973), and improved in 1983 (Wang, 1983). It is an unsupervised fuzzy clustering method and its steps are as follows (Pessoa

251 et al., 2018):

252   1) Choose the number of clusters c. The optimum number of clusters is determined by $L(c)$, which is derived from the inter-

253 distance and inner distance of the samples in Eq. (2). It is ensured that the distance between similar samples is smaller, while

254 the distance between different samples is larger.

$$L(c) = \frac{\sum_{i=1}^{c}\sum_{j=1}^{n} w_{ij}^{m} \| c_i - \overline{x} \|^2 /(c-1)}{\sum_{i=1}^{c}\sum_{j=1}^{n} w_{ij}^{m} \| x_j - c_i \|^2 /(n-c)} \tag{2}$$

256   In Eq. (2), the denominator is the inner-distance, and the numerator is the inter-distance. The initial value of c is 1 and the

257 maximum value of c is the number of gauge stations in the study area. The optimum number of clusters was optimized to

258 maximize L(c). For this reason, the value of c is varied from 1 to the number of gauge stations with an increment of 1 in this

259 study.

260   2) Assign coefficients randomly to each data point x_i for the degree to which it belongs in the i-th cluster $w_{ij}(x_i)$:

$$c_i^{(t)} = \frac{\sum_{j=1}^{n} w_{ij}^{m} x_i}{\sum_{j=1}^{n} w_{ij}^{m}} \quad (3), \qquad w_{ij} = \frac{1}{\sum_{k=1}^{c}(\frac{\| x_i - c_i \|}{\| x_i - c_k \|})^{\frac{2}{m-1}}} \quad (4), \qquad \overline{x} = \frac{\sum_{i=1}^{c}\sum_{j=1}^{n} w_{ij}^{m} x_j}{n} \quad (5)$$

262 where x is a finite collection of n elements that will be partitioned into a collection of c fuzzy clusters, c_i is the centre of

263 each cluster, m is the hyper-parameter that controls the level of cluster fuzziness, w_{ij} is the degree to which element x_i

264 belongs to c_i, and $\overline{x}$ is the centre vector of the collection. In Eq. (3), $c_j^{(t)}$ represents the cluster centre in iteration t. If the

265 minimum improvement in the objective function between two consecutive iterations satisfies the following equation, the

algorithm terminates in iteration t (Eq. (6)):

$$\|c_i^{(t)} - c_i^{(t+1)}\| < \varepsilon \tag{6}$$

3) Minimize the objective function F_c to achieve data partitioning.

$$F_c = \sum_{j=1}^{n}\sum_{i=1}^{c} w_{ij}^{m} \| x_j - c_i \|^2 \tag{7}$$

The results of the FCM are the degree of membership of each pixel to the cluster centre as represented by numerical values. The pixels in each cluster have similar terrain features and precipitation characteristics.

Second, as mentioned above, the aim of Rule 2 is to derive an adjustment method for the C2 pixels based on learning from Rule 1. With the establishment of a regression relationship between the gauge observations and the corresponding CHIRP grid cell values of the C1 pixels by the RFR method, the determination of the C2 pixels follows a complicated procedure. With the exception of the C1 pixels, the remaining pixels in each cluster represent potential C2 pixels, which are called R pixels. The Pearson's correlation coefficient (PCC) and p-values between the satellite estimations (multi-year daily CHIRP grid cell values) at the R pixels and the C1 pixels are the criteria for the final determination of the C2 pixels. The PCC is defined as follows:

$$PCC_{x,y} = \frac{\sum_{i=1}^{n}(x_i - \bar{x})(y_i - \bar{y})}{\sqrt{\sum_{i=1}^{n}(x_i - \bar{x})^2}\sqrt{\sum_{i=1}^{n}(y_i - \bar{y})^2}} \tag{8}$$

where n is the number of samples, x_i and y_i are individual samples (CHIRP grid cell values at the C1 and C2 pixels, respectively), $\bar{x}$ is the arithmetic mean of x calculated by $\bar{x} = \frac{1}{n}\sum_{i=1}^{n} x_i$, and $\bar{y}$ is the arithmetic mean of y calculated by

$$\bar{y} = \frac{1}{n}\sum_{i=1}^{n} y_i.$$

The PCC ranges between -1 and +1. If there are no repeated data values, a perfect PCC of +1 or −1 occurs when each of the variables is a perfect monotonic function of the other. However, if the value is close to zero, there is zero correlation. In addition, the correlation is not only determined by the value of the correlation coefficient but also by the correlation test's p-value. The critical values for the PCC and p-value are 0.5 and 0.05, respectively; thus, a PCC value higher than 0.5 and a p-value lower than 0.05 indicate that the data are significantly correlated (Zhang and Chen, 2016). Therefore, the final determination of the C2 pixels must meet the following criteria:

$$|PCC| \geq 0.5 \quad and \quad p < 0.05 \tag{9}$$

Each R pixel has m PCC and p-values (the number of C1 pixels in the cluster), and the subset of C2 pixels is identified by excluding the data that failed the correlation test and retaining both the data with a maximum PCC of at least 0.5 and a p-value lower than 0.05, and the corresponding index of C1 pixels. The selected C2 pixels can then be considered statistically similar to the precipitation characteristics of the corresponding C1 pixels in their defined spatial area.

After identifying the C2 pixels and their corresponding C1 pixels, the adjustment method for the C2 pixels is derived from the regression model for the C1 pixels:

$$C2_{as} = \frac{1}{n}\sum_{k=1}^{n} Tree_{k_{C1}}(Y_{s_{C2}}) \tag{10}$$

where $Tree_{k_{C1}}$ is the decision tree derived from the RFR algorithm at the corresponding C1 pixel, $Y_{s_{C2}}$ is the CHIRP grid cell value at the C2 pixels, and $C2_{as}$ is the adjusted satellite precipitation estimate calculated by the average of the values from the RFR decision trees.

3.1.4 Rule 3 of the WHU-SGCC method

Recognizing that precipitation has a spatial distribution, the assumption that the C3 pixels are statistically similar to the precipitation characteristics of the C2 pixels is adopted to establish the adjustment method for the C3 pixels.

First, the determination of the C3 pixels in each spatial cluster is based on the selection of C2 pixels. The satellite-based estimation values at the pixels other than the C1 and C2 pixels are used to calculate the PCC and p-value with the satellite-based estimation values at the C2 pixels in the same cluster. The results of each pixel's k PCC and p-value (the number of C2 pixels in the cluster) are evaluated based on the correlation test (Eq. (9)) that the pixels have a maximum PCC of at least 0.5 and a p-value is of no more than 0.05, and the corresponding index of C2 pixels is retained. The selected pixels are called C3 pixels, which are statistically similar to the precipitation characteristics of the corresponding C2 pixels in the defined spatial area.

After identifying the C3 pixels, a method for merging the CHIRP grid cell values at the C3 pixels (Y_S) and the target reference values of $C2_{as}$ at the corresponding C2 pixels is applied to estimate the adjusted precipitation values at the C3 pixels. This method combines the Y_S and $C2_{as}$ values into one variable, as shown in Eq. (11):

$$w_i = \frac{C2_{as_i} + \lambda}{Y_{s_i} + \lambda} \quad i=1,\ldots,\ n \tag{11}$$

where λ is a positive constant set to 10 mm (Sokol, 2003), $C2_{as}$ is the adjusted precipitation values at the C2 pixels, Y_{s_i} is extracted from the CHIRP grid cell values at the corresponding location of the C2 pixels, and n is the number of C2 pixels in each spatial cluster.

Each w of the C3 pixels is assigned the same value as the corresponding C2 pixel. Therefore, the values of the C3 pixels are derived from Eq. (12):

$$C3_{as} = \max(w \times (Y_s + \lambda) - \lambda, 0) \tag{12}$$

where $C3_{as}$ is the adjusted target precipitation value at one C3 pixel, and Y_s is the corresponding CHIRP grid cell value. To avoid precipitation estimates below 0, Eq. (12) sets negative values to 0.

3.1.5 Rule 4 of the WHU-SGCC method

The pixels other than the C1, C2 and C3 pixels are called C4 pixels and they are adjusted by inverse distance weighting (IDW). IDW is based on the concept of the first law of geography from 1970, which was defined as *everything is related to everything else, but near things are more related than distant things*. Therefore, the attribute value of an unsampled point is the weighted average of the known values within the neighbourhood, and the distance weighting can be determined by means of IDW (Lu and Wong, 2008). In Rule 4, IDW is used to interpolate the unknown spatial precipitation data from the adjusted precipitation values at the C2 and C3 pixels. The IDW formulas are given as Eq. (13) and Eq. (14).

$$R_{as} = \sum_{i=1}^{n} w_i R_i \tag{13}$$

$$w_i = \frac{d_i^{-\alpha}}{\sum_{i=1}^{n} d_i^{-\alpha}} \quad \text{with} \ \sum_{i=1}^{n} w_i = 1 \tag{14}$$

where R_{as} is the unknown spatial precipitation data, R_i is the adjusted precipitation values at the C2 and C3 pixels, n is the number of C2 and C3 pixels, d_i is the distance from each C2 or C3 pixel to the unknown grid cell, and α is the power which

333 is generally specified as a geometric form for the weight. Several studies (Simanton and Osborn 1980; Tung 1983) have

334 experimented with variations in the power; a the small α tends to estimate values with the averages of sampled grids in the

335 neighbourhood, while a large α tends to give larger weights to the nearest points and increasingly down-weights points

336 farther away (Chen and Liu, 2012;Lu and Wong, 2008). The value of α has an influence on the spatial distribution of the

337 information from precipitation observations. For this reason, α is varied in the range of 0.1 to three (0.1, 0.3, 0.5, 1.0, 1.5,

338 2.0, 2.5 and 3.0) in this study.

339 Note that the unknown spatial precipitation data include C1 and C4 pixels because the C1 pixels values were not adjusted

340 in Rule 1.

341 After applying these four rules, we obtained complete daily adjusted regional precipitation maps for the four seasons over

342 the Jinsha River basin.

3.2 Accuracy assessment

344 The performance of the WHU-SGCC adjusted precipitation estimates was evaluated by eight mathematic metrics: the

345 Pearson's correlation coefficient (PCC), root mean square error (RMSE), mean absolute error (MAE), relative bias (BIAS),

346 Nash-Sutcliffe efficiency coefficient (NSE), probability of detection (POD), false alarm ratio (FAR) and critical success index

347 (CSI). The results of accuracy assessment are the average values validated by the leave-one-out cross method. Each validated

348 pixel will probably be a C2, C3 or C4 pixel in the process of the WHU-SGCC algorithm. The PCC, RMSE, MAE and BIAS

349 were used to evaluate how well the WHU-SGCC method adjusted the satellite estimation bias, while POD, FAR and CSI were

350 used to evaluate the performance of precipitation forecasting (Su et al., 2011). The PCC measures the strength of the correlation

351 relationship between the satellite estimations and observations. The RMSE is an absolute measurement used to compare the

352 difference between the satellite estimations and observations, and the MAE represents the average magnitude of error

353 estimations considering both systematic and random errors. The NSE (Nash and Sutcliffe, 1970) determines the relative

354 magnitude of the variance of the residuals compared to the variance of the observations, bounded by minus infinity and 1; a

355 negative value indicates a poor precipitation estimate, and a value of1 indicates an optimal estimate. The BIAS measures the

356 mean tendency of the estimated precipitation to be larger (positive values) or smaller (negative values) than the observed

357 precipitation and has an optimal value of 0. The POD, also known as the hit rate, represents the probability of rainfall detection,

358 and the FAR is defined as the ratio of the false alarm of rainfall to the total number of rainfall events. All of the accuracy

359 assessment metrics are shown in Table 2.

360

Table 2 Accuracy assessment metrics.

Accuracy assessment Index	Unit	Formula	Range	Optimal value
Pearson's Correlation Coefficient (PCC)	NA	$PCC = \dfrac{\sum_{i=1}^{n}(Y_{oi} - \bar{Y}_o)(C_i - \bar{C})}{\sqrt{\sum_{i=1}^{n}(Y_{oi} - \bar{Y}_o)^2} \cdot \sqrt{\sum_{i=1}^{n}(C_i - \bar{C})^2}}$	[-1,1]	1
Root Mean Square Error (RMSE)	mm	$RMSE = \sqrt{\dfrac{1}{n}\sum_{i=1}^{n}(C_i - Y_{oi})^2}$	[0,+∞)	0
Mean Absolute Error (MAE)	mm	$MAE = \dfrac{1}{n}\sum_{i=1}^{n}|C_i - Y_{oi}|$	[0, +∞)	0
Relative Bias (BIAS)	NA	$BIAS = \dfrac{\sum_{i=1}^{n}(C_i - Y_{oi})}{\sum_{i=1}^{n} Y_{oi}}$	(-∞, +∞)	0
Nash-Sutcliffe Efficiency Coefficient (*NSE*)	NA	$NSE = 1 - \dfrac{\sum_{i=1}^{N}(C_i - Y_{oi})^2}{\sum_{i=1}^{N}(C_i - \bar{Y}_o)^2}$	(-∞,1]	1
Probability of Detection (POD)	NA	$POD=H/(H+M)$	[0,1]	1
False Alarm Ratio (FAR)	NA	$FAR=F/(H+F)$	[0,1]	0
Critical Success Index (CSI)	NA	$CSI=H/(H+M+F)$	[0,1]	1

361 Note: Y_{oi} is the observation data; C_i is the adjusted value using the WHU-SGCC method for the test sample pixel; $\bar{Y}_o$ is

362 the arithmetic mean of Y_o and is given by $\overline{Y}_o = \frac{1}{n}\sum_{i=1}^{n} Y_{oi}$; $\overline{C}$ is the arithmetic mean of C and is given by $\overline{C} = \frac{1}{n}\sum_{i=1}^{n} C_i$; H

363 represents the number of both observed and estimated precipitation events (successfully forecasted); F is the number of false

364 alarms when the observed precipitation was below the threshold and estimated precipitation was above threshold (false alarms;

365 and. M is the number of events in which the estimated precipitation was below the threshold and observed precipitation was

366 above the threshold (missed forecasts). The POD and FAR values are dimensionless numbers ranging from 0 to 1. The

367 precipitation threshold (event/no event) was set to 0.1 mm/day.

368 **4 Results and Discussion**

369 A total of 18,482 daily pixels were adjusted by blending the satellite estimations (CHIRP) and observations (rain gauge stations)

370 using the WHU-SGCC approach over the Jinsha River Basin from 1990 to 2014. The percentage of pixels adjusted by each

371 rule in the WHU-SGCC method is shown in Table 3. The number of C1 pixels was the number of training gauge stations,

372 which accounted for 0.16% of the total pixels (18,482) within the basin. Due to the leave-one-out cross validation step, the

373 different training samples will have different numbers of C2, C3 and C4 pixels within the Jinsha River Basin. The percentage

374 of C2 and C3 pixels are highest in fall, followed by summer, spring and winter. In the spring, the average percentage of C2

375 pixels was approximately 21%, the average percentage of C3 pixels was approximately 17%, and the percentage of C4 pixels

376 was approximately 61%. In the summer, the percentage of C2 pixels was ranging from 15.59% to 18.36%, the percentage of

377 C3 pixels was ranging from 21.72% to 24.40%, and the percentage of C4 pixels was approximately 60%. In the full, the

378 average percentage of C2 pixels was approximately 31%, the average percentage of C3 pixels was approximately 22%, and

379 the average percentage of C4 pixels was approximately 47%. In the winter, the average percentage of C2 pixels was

380 approximately 16%, the average percentage of C3 pixels was approximately 19%, and the average percentage of C4 pixels

381 was approximately 65%. Besides, the pixel type of the validation gauge station is shown in Table D1. Each validation gauge

382 station could be identified as either C2, C3 or C4 pixels to evaluate the performances of all the rules in the WHU-SGCC

383 method.

384 **Table 3** The percentage of each class pixels adjusted by each rule using the WHU-SGCC method within the Jinsha River Basin.

Validation gauge station	C2 Pixels (%)				C3 Pixels (%)				C4 Pixels (%)			
	Spring	Summer	Fall	Winter	Spring	Summer	Fall	Winter	Spring	Summer	Fall	Winter
52908	20.80%	16.59%	29.15%	15.52%	17.76%	22.85%	20.82%	18.16%	61.29%	60.40%	49.87%	66.16%
56004	20.89%	15.59%	29.40%	15.65%	16.29%	22.24%	20.64%	18.83%	62.66%	62.01%	49.81%	65.36%
56021	21.38%	17.91%	32.46%	15.65%	17.55%	24.40%	21.85%	19.91%	60.91%	57.53%	45.53%	64.28%
56029	21.77%	18.06%	32.60%	16.03%	17.31%	24.06%	21.61%	19.64%	60.76%	57.72%	45.63%	64.18%
56034	21.09%	17.86%	31.22%	14.86%	17.78%	23.95%	23.07%	20.19%	60.97%	58.03%	45.55%	64.79%
56038	20.48%	17.36%	30.72%	15.56%	16.12%	21.72%	23.74%	17.63%	63.23%	60.76%	45.39%	66.65%
56144	21.42%	18.11%	31.97%	16.00%	16.46%	24.03%	21.78%	19.38%	61.96%	57.70%	46.09%	64.46%
56146	21.33%	17.22%	31.77%	15.70%	17.12%	24.24%	21.42%	18.34%	61.39%	58.38%	46.65%	65.81%
56152	21.32%	17.17%	31.27%	15.57%	17.56%	22.59%	22.32%	18.94%	60.96%	60.08%	46.26%	65.34%
56167	21.46%	18.19%	32.36%	15.84%	16.90%	23.51%	21.72%	19.03%	61.48%	58.14%	45.76%	64.98%
56247	21.66%	18.32%	31.44%	16.10%	17.16%	23.89%	22.19%	19.55%	61.03%	57.63%	46.21%	64.20%
56251	21.09%	17.86%	31.28%	15.73%	17.39%	23.53%	22.88%	18.50%	61.36%	58.46%	45.68%	65.62%
56257	21.17%	17.93%	30.99%	15.95%	16.15%	21.88%	23.55%	19.13%	62.53%	60.04%	45.30%	64.77%
56357	21.62%	18.14%	31.59%	15.64%	17.12%	23.75%	22.54%	19.52%	61.10%	57.95%	45.71%	64.68%
56374	21.52%	18.08%	31.92%	14.32%	17.38%	23.23%	21.90%	19.20%	60.95%	58.53%	46.02%	66.32%
56459	21.30%	18.10%	32.14%	15.64%	16.92%	23.45%	21.16%	19.17%	61.62%	58.29%	46.54%	65.03%
56462	21.67%	18.29%	32.68%	15.92%	17.28%	23.68%	21.55%	19.14%	60.90%	57.87%	45.61%	64.78%

56475	21.49%	18.10%	32.49%	15.98%	16.36%	23.50%	22.08%	19.53%	62.00%	58.24%	45.28%	64.33%
56479	20.42%	17.88%	31.34%	15.69%	16.35%	22.79%	19.36%	18.74%	63.07%	59.17%	49.14%	65.41%
56485	21.44%	18.36%	32.78%	15.64%	17.43%	23.91%	21.82%	19.85%	60.97%	57.57%	45.24%	64.35%
56543	21.52%	18.25%	32.51%	15.87%	16.97%	23.72%	21.78%	18.90%	61.35%	57.87%	45.56%	65.06%
56565	21.21%	17.54%	30.93%	15.52%	17.81%	24.08%	23.55%	19.96%	60.83%	58.23%	45.36%	64.37%
56571	21.62%	17.89%	31.31%	14.94%	17.03%	23.07%	20.83%	18.94%	61.19%	58.89%	47.70%	65.97%
56586	21.73%	18.33%	21.73%	15.49%	17.35%	23.99%	17.35%	19.59%	60.76%	57.53%	60.76%	64.77%
56651	20.90%	18.07%	32.46%	15.38%	17.78%	23.98%	22.13%	19.95%	61.16%	57.79%	45.25%	64.51%
56664	20.94%	18.22%	32.43%	15.50%	16.64%	23.06%	21.00%	18.70%	62.26%	58.56%	46.42%	65.64%
56666	21.06%	17.98%	31.59%	15.39%	18.03%	23.97%	22.41%	19.64%	60.76%	57.89%	45.84%	64.82%
56671	20.71%	18.16%	32.55%	15.67%	16.53%	23.63%	21.89%	20.03%	62.61%	58.06%	45.41%	64.14%
56684	21.36%	18.04%	32.65%	15.46%	17.72%	23.15%	21.95%	19.28%	60.76%	58.65%	45.24%	65.10%
56778	21.63%	18.11%	32.25%	15.91%	17.31%	23.14%	22.11%	19.52%	60.90%	58.59%	45.48%	64.41%

385

4.1 Model performance based on overall accuracy evaluations

The multi-year (1990-2014) average seasonal precipitation over the Jinsha River Basin interpolated from WHU-SGCC, CHIRP and CHIRPS is shown in Fig. 4. There exist some differences in the spatial pattern of precipitation estimates. Overall, the WHU-SGCC method exhibits the similar spatial distribution of precipitation to the CHIRP and CHIRPS, while the WHU-SGCC method attenuated the intense rain in the central area. The statistical accuracy evaluations are needed to further analyze the performance of the WHU-SGCC method.
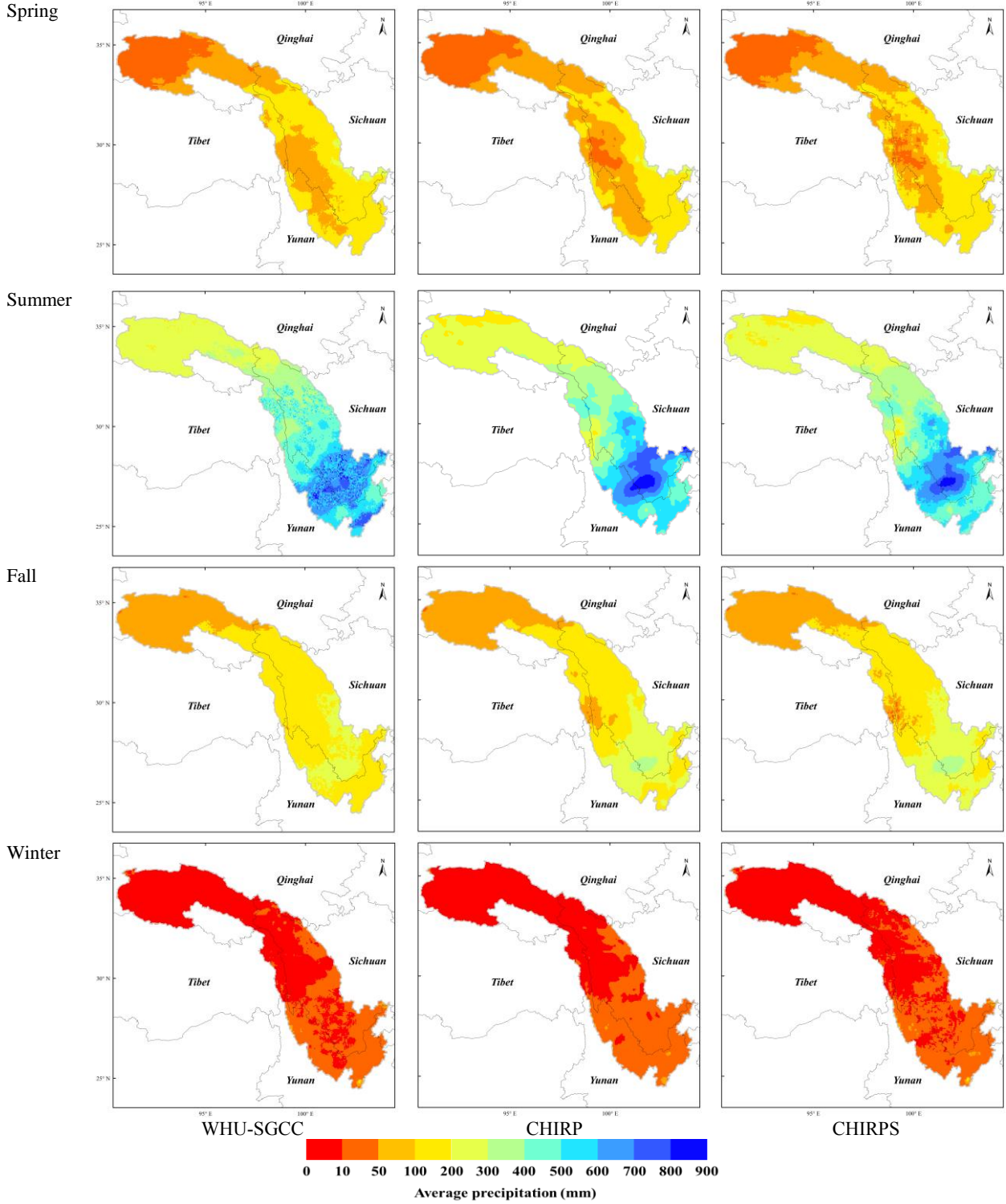
Figure 4 The multi-year (1990-2014) average seasonal precipitation over the Jinsha River Basin interpolated from WHU-SGCC, CHIRP and CHIRPS.

To test the performance of the WHU-SGCC method for precipitation estimates, the PCC, RMSE, BAE, BIAS, NSE, POD,

FAR, and CSI were calculated and are presented in Table 4 (the results were derived from the 22 clusters for the FCM in Rule 2, as shown in Appendix E, and α =0.1 for the IDW in Rule 4 after the comparison of the RMSE). After the correction, the PCC in the WHU-SGCC method shows an improvement relative to the CHIRP and CHIRPS estimates. The spring and fall have better correlations than the summer and winter. In addition, the NSE of the WHU-SGCC provides substantial improvements over CHIRP and CHIRPS, especially in the spring and fall which were better than the summer and winter. The RMSE and MAE are the largest in the summer, followed by the fall, spring, and winter; however, the performances of the BIAS in the summer and fall are better than those in the spring and winter, which might be influenced by the greater precipitation in the summer and fall than in the spring and winter. The assessments of the POD and CSI are lowest, and the FAR is largest in the winter due to the overestimation of no rain events estimated by the satellite-based data set.

Compared with the estimates of CHIRP and CHIRPS, the PCCs of the WHU-SGCC method are improved to more than 0.5 in the spring and fall and to approximately to 0.5 in the winter. In addition, the RMSE and MAE of the WHU-SGCC were all lower than those of CHIRP and CHIRPS. The absolute values of the BIAS of the WHU-SGCC are substantial improved in the spring, followed by the summer, winter and fall. Although the absolute value of the BIAS of the WHU-SGCC in fall are not significantly better than those of CHIRP and CHIRPS, all of the values are approximately 0. The NSEs of the WHU-SGCC reached 0.2836, 0.2944 and 0.1853 in the spring, fall and winter, respectively, which are substantially better than the negative or zero values of CHIRP and CHIRPS. In the summer, the NSE of the WHU-SGCC is still negative, but it is improved to be nearly zero, which indicates that the adjusted results are similar to the average level of the rain gauge observations. It is worth noting that in the spring, summer and fall, the POD values of the WHU-SGCC are in the range of 0.95 to 1, better than CHIRP and CHIRPS, and the FAR values of the WHU-SGCC are no more than 0.3, lower than CHIRP and CHIRPS; these results represent the better ability of the WHU-SGCC method to predict precipitation events. The rainfall detection ability is the worst in the winter compared to the other seasons. This can be explained by the seasonal distribution of precipitation in the Jinsha River Basin, in which the most rainfall occurs in the summer, followed by the fall, spring and winter. In addition, the spatial distribution of C2 and C3 pixels also significantly impact the overall accuracy in different seasons that the most uniform in the fall, while the sparsest in the winter. The worst errors of forecasting performance in the summer may be attributed to the highest precipitation. The limited precipitation event detection in the winter could also be explained by the lowest precipitation (Xu et al., 2019).

Table 4 Overall accuracy assessments for the four seasons from 1990 to 2014.

Statistic	Spring			Summer			Fall			Winter		
	WHU-SGCC	CHIRP	CHIRPS	WHU-SGCC	CHIRP	CHIRPS	WHU-SGCC	CHIRP	CHIRPS	WHU-SGCC	CHIRP	CHIRPS
PCC	0.5376	0.3644	0.2132	0.2536	0.2454	0.1924	0.5508	0.3889	0.2661	0.4722	0.2490	0.1716
RMSE	2.9526	3.4332	5.1926	8.7608	9.4108	11.3354	4.7981	4.9038	7.7506	0.8120	0.9042	1.0569
MAE	1.3380	1.5426	1.9948	5.4564	5.8415	7.0088	2.0973	2.2943	2.9925	0.2093	0.7398	0.6905
BIAS	-0.1148	-0.2490	-0.1783	-0.0167	-0.0443	-0.0134	-0.0566	-0.0563	-0.0231	-0.1775	-0.2083	-0.3093
NSE	0.2836	0.0745	-1.0817	-0.0139	-0.2083	-0.8293	0.2944	0.0168	-1.4692	0.1853	0.0161	-0.3098
POD	0.9605	0.8572	0.2918	0.9932	0.9578	0.4351	0.9612	0.9047	0.2326	0.6988	0.5786	0.2076
FAR	0.2416	0.4515	0.3888	0.1146	0.2323	0.1601	0.2386	0.4301	0.2638	0.5242	0.7082	0.6381
CSI	0.6928	0.5001	0.2335	0.8799	0.7405	0.401	0.7089	0.5303	0.2144	0.3668	0.2210	0.1352

The spatial distributions of the statistical comparisons between the observations and the WHU-SGCC precipitation estimations are shown in Fig. 5 and Fig. 6. Overall, the variation in the PCC shows low correlations in areas with lower elevation, particularly in the southeast Jinsha River Basin, where there is higher precipitation and a greater density of rain gauges. The PCC is highest in the fall, followed by the spring and winter, and finally by summer. The higher correlations are located in the north-central area along the Tongtian River, Jinsha River and upstream part of the Yalong River, which has complex terrain and few rain gauges. The RMSE is lowest in the winter than in the spring, fall and summer, which can be

attributed to the lower precipitation in the winter and the greatest in the summer. The spatial distribution of the RMSE shows that, the smaller errors are scattered in the northwest area of the river basin, with values lower than 5 mm, while the highest errors are located along the border between the lower reaches of the Jinsha Jiang River and the river basin. This is related to the climate regimes of the Jinsha River Basin, which includes more rainfall in the south and southeast areas than in the north, and northwest.

The results show that the WHU-SGCC method improves the correlation relative to CHIRP and CHIRPS, especially in central and southeast river basin during the spring, fall and winter, with most of the PCC values falling between 0.4 and 0.8 (Fig. 5). As shown by the RMSE (Fig. 6), the WHU-SGCC can also correct the precipitation errors in the central and southeast river basin, especially along the downstream part of the Yalong River. In addition, the WHU-SGCC slightly improved the RMSE around the convergence of the rivers, where it is less than 5 mm in the spring and fall, and most of RMSE values are less than 1 mm in the winter. In spite of the correction, the RMSE values in the summer are still substantial.

All of the spatial distribution statistics indicate that the statistical relationships established during the process of the WHU-SGCC method are susceptible to the mode values of the rain gauge stations data, especially in the summer. Although the average summer precipitation in the southern Jinsha River Basin was more than 600 mm (Fig. 2), days of light rain still represent a large percentage, which causes large biases and limits the performance over the south, while there are sufficient data with similar precipitation features for the WHU-SGCC in the north. Nevertheless, the WHU-SGCC approach is still effective at adjusting the satellite biases by blending the data with the observations, particularly in the complicated mountainous regions, where higher PCCs correspond to lower RMSEs.

Winter

WHU-SGCC   CHIRP   CHIRPS

0   0.2 0.3 0.4 0.5 0.6 0.8 1.0
Pearson's correlation coefficient
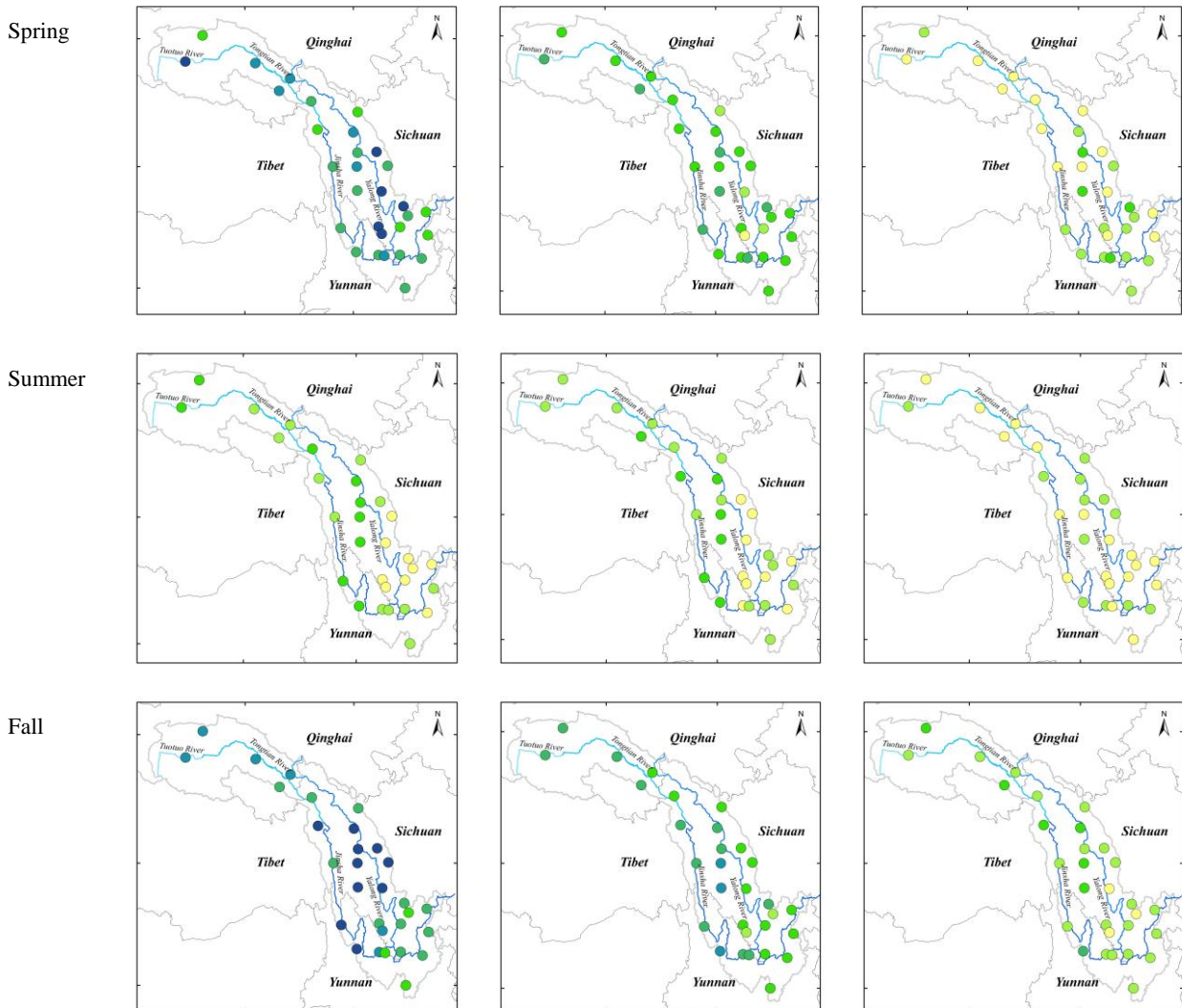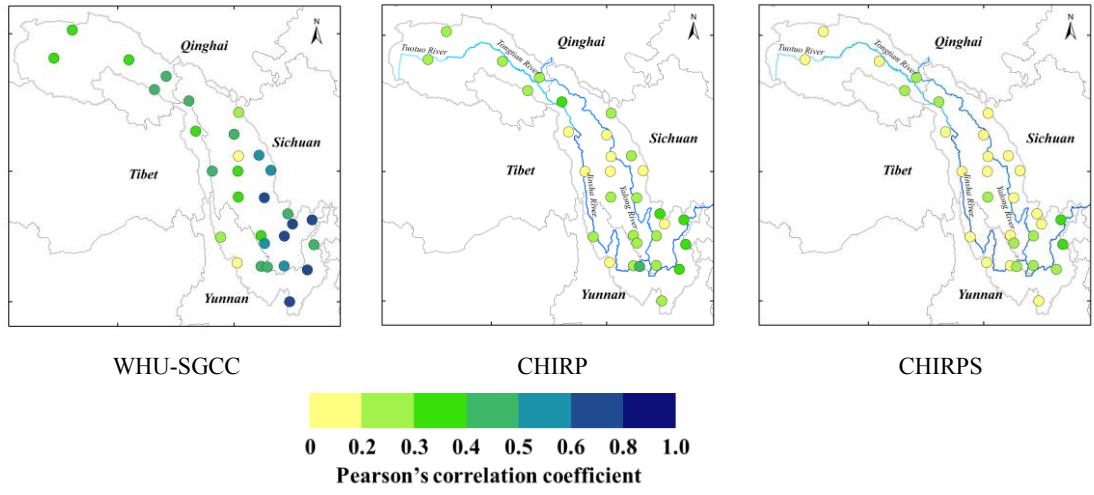
447
448   **Figure 5** Spatial distribution of the Pearson's correlation coefficient of the overall agreement between observations and the WHU-SGCC,
449   CHIRP and CHIRPS estimations in the four seasons from 1990 to 2014.

Spring

Summer

Fall

Winter

| WHU-SGCC | CHIRP | CHIRPS |

Root mean square error

0   1   3   5   10   15   20
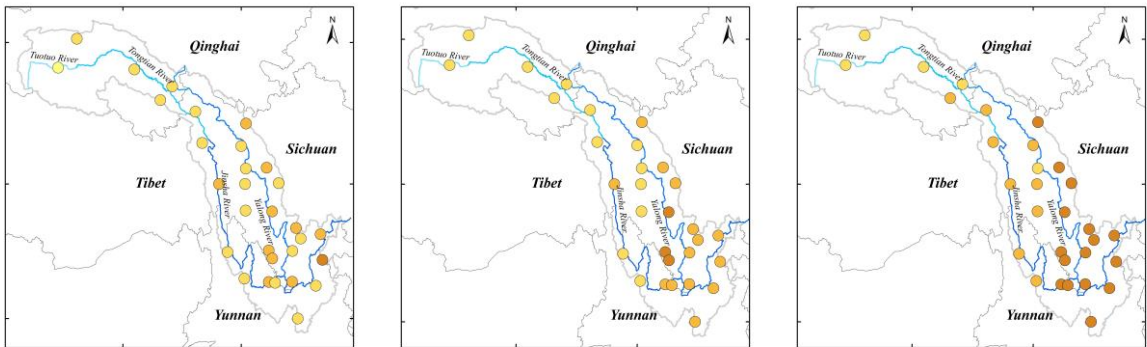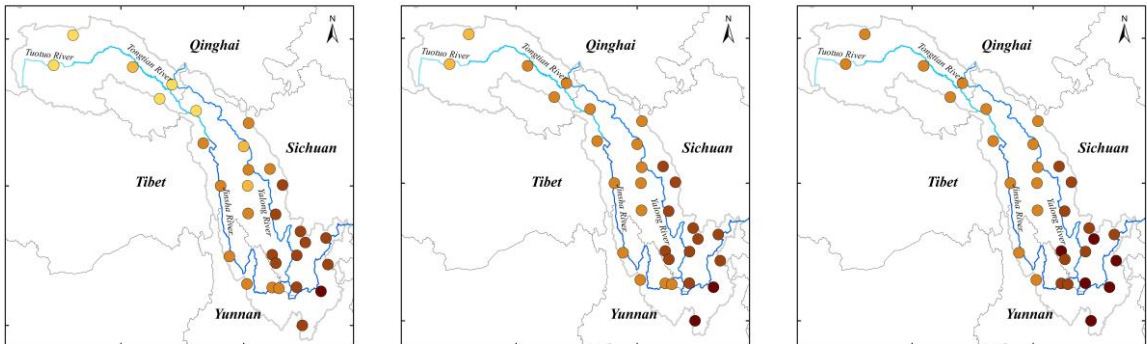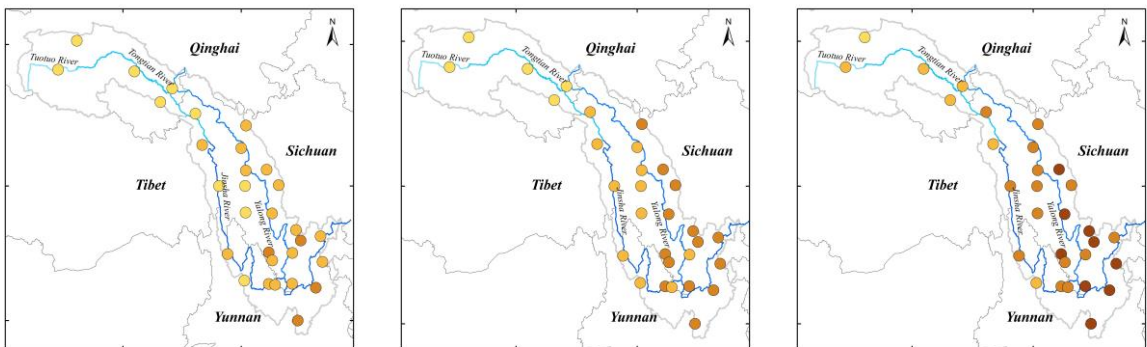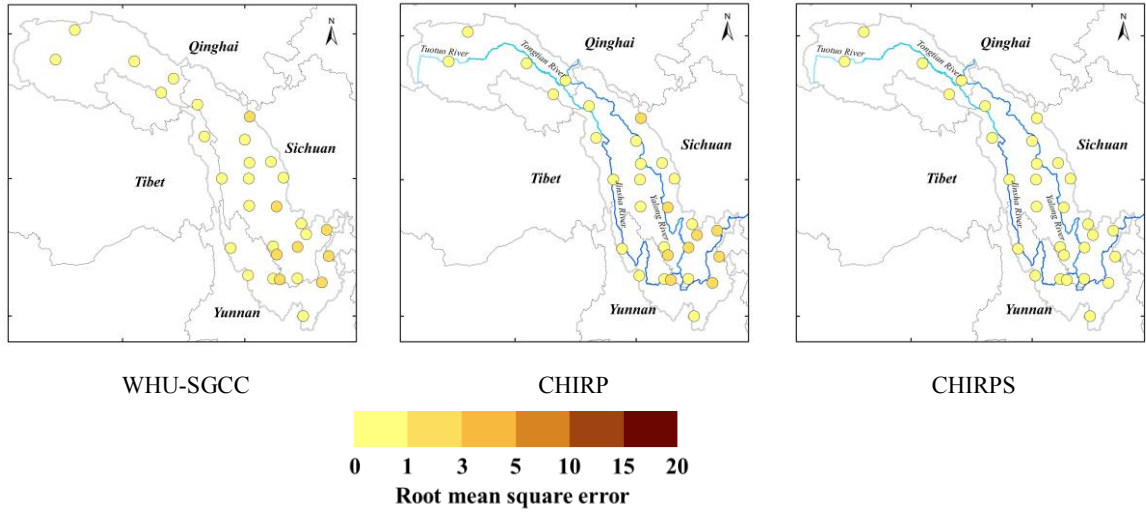
Figure 6 Spatial distribution of the root mean square errors of the overall agreement between observations and the WHU-SGCC, CHIRP and CHIRPS estimations in the four seasons from 1990 to 2014.

4.2 Model performance based on daily accuracy evaluations

After the overall accuracy evaluations were conducted, further evaluations of the daily accuracy in the four seasons were conducted, and the results are shown in Fig. 7. The evaluation of the daily accuracy indicates that the PCCs of the WHU-SGCC were slightly better than those of CHIRP and CHIRPS in the spring, fall and winter but were not as good in the summer and winter. The WHU-SGCC had lower RMSEs and MAEs than CHIRP and CHIRPS, especially compared to CHIRPS. The daily RMSE and MAE in the summer are the highest, although the WHU-SGCC still corrects the errors. Figure 7 indicates that there is a slight increase in the PCC, with average improvements of 0.02-0.04 and 0.04-0.14, respectively; however, the PCC is a relative metric of the magnitude of the association between paired variables, and a relative consistency may not indicate absolute proximity. Thus, the absolute measure indicated by the RMSE may be more reasonable. In this study, the RMSE and MAE derived from the WHU-SGCC are reduced by approximately 15% and 34% on average compared to CHIRP and CHIRPS, respectively. As for BIAS, WHU-SGCC method can correct the CHIRP precipitation bias in the spring, fall and winter, but the results are not as good compared with CHIRPS. The larger BIAS values and higher PCCs in the spring and fall may be attributed to the seasonal variations, when the CHIRP is highly consistent with the observations but subject to large biases. After the correction, a substantial decrease in BIAS occurs in the winter, and there is no significant reduction in the summer; all of the median and average adjusted values are approximately 0. The WHU-SGCC method provides an obvious improvement in the NSE relative to CHIRP and CHIRPS, though the median and average values are still less than 0, which may be due to the inherent uncertainty in the CHIRP. Moreover, in terms of the POD, FAR and CSI, except for the results in winter, the WHU-SGCC method appears to be better at detecting precipitation than CHIRP and CHIRPS; the results of POD and CSI are closest to 1, although FAR is worse than CHIRPS on some days. However, the overall result of FAR is the best in the WHU-SGCC. The POD and FAR results are the worst in the winter, and the CSI is slightly higher, which may be attributed to the overestimation of no-rain events and the inherent uncertainty in the CHIRP.

Overall, the WHU-SGCC approach can be regarded as an effective tool for daily precipitation adjustments.

475

476

477

478

(a) PCC

(b) RMSE

(c) MAE

(d) BIAS

479

480

481

482
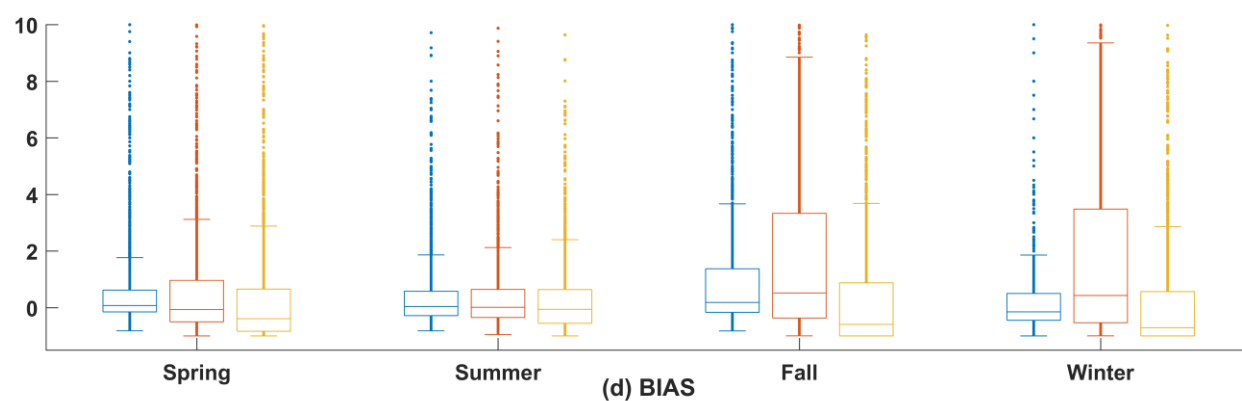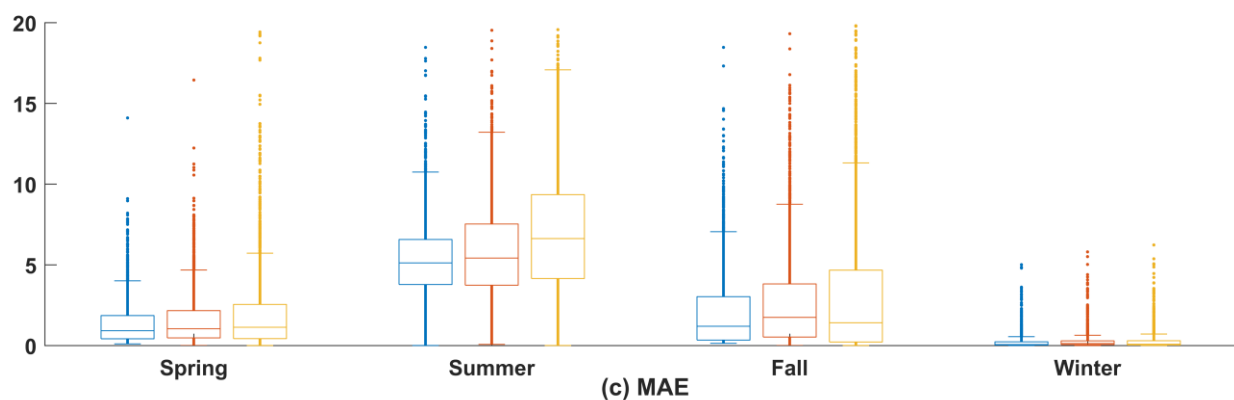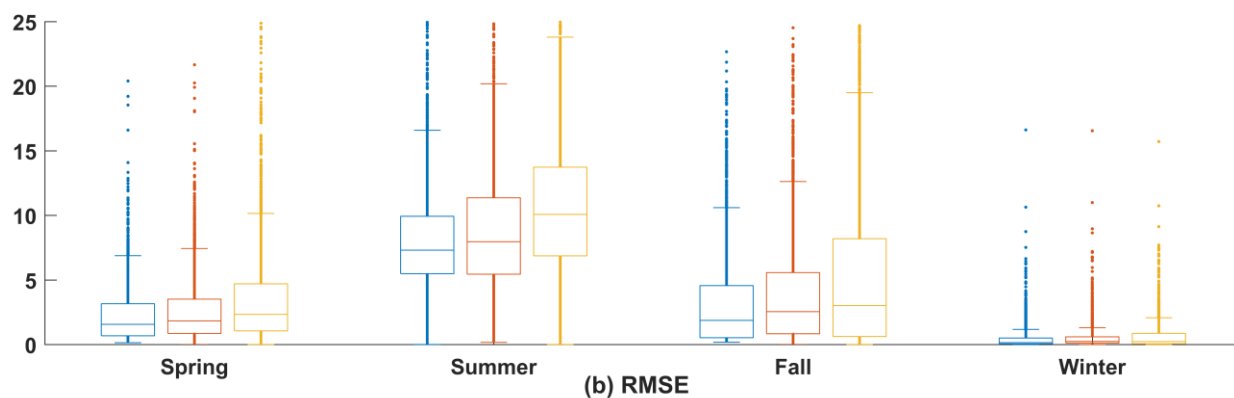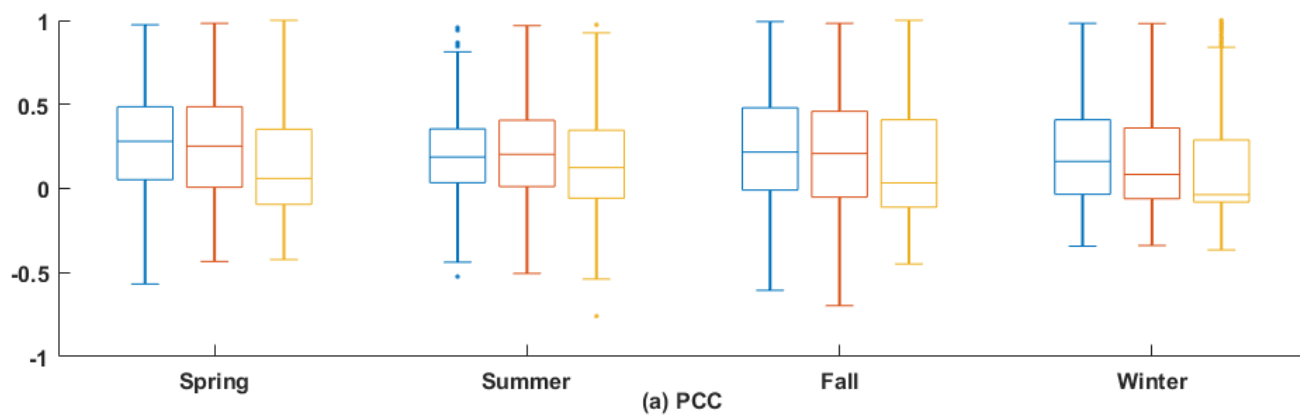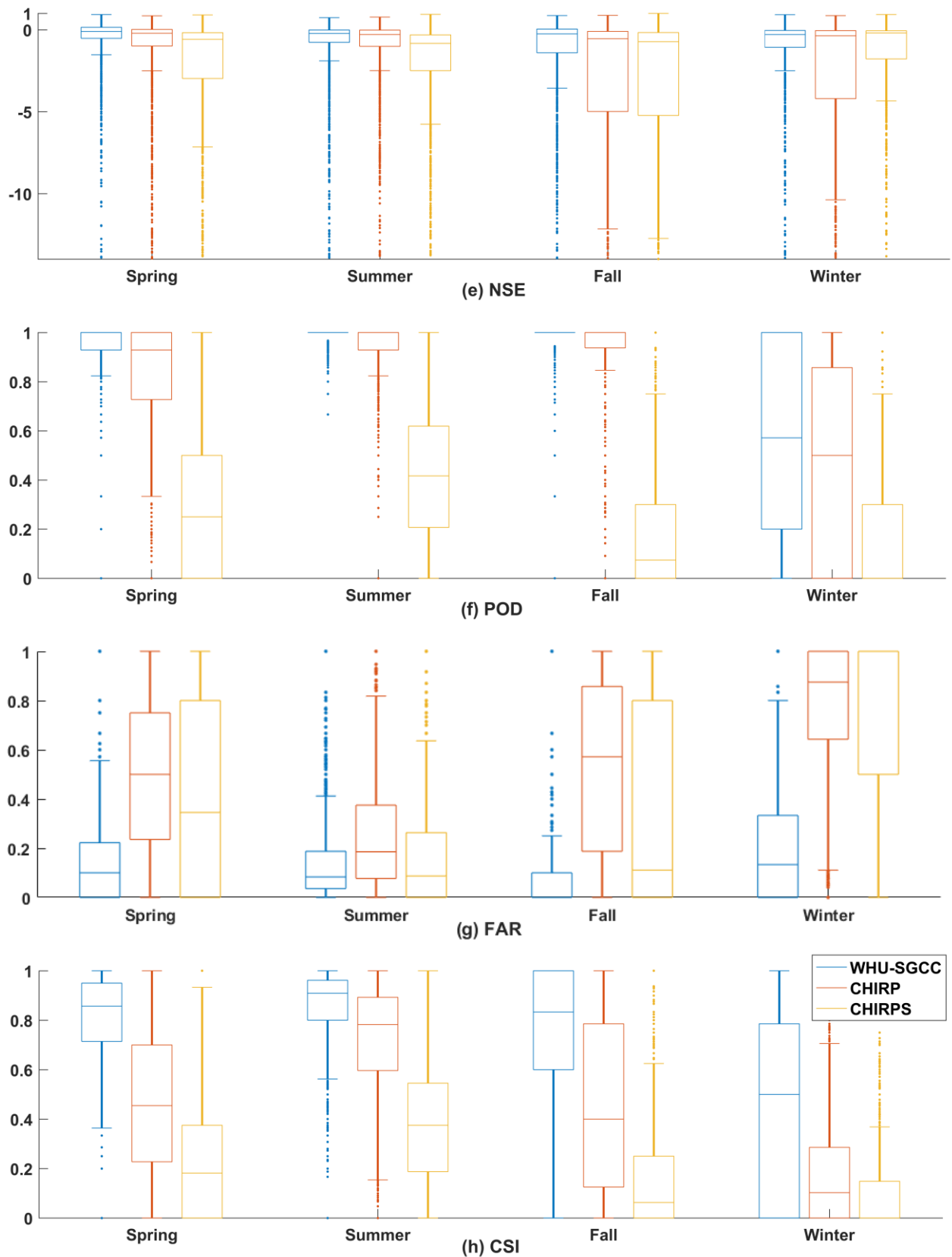
483 **Figure 7** Statistical analysis of the agreement between the daily observations and the WHU-SGCC, CHIRP and CHIRPS estimates with the
484 leave-one-out cross validation: a) Pearson's correlation coefficient, b) root mean square error, c) mean absolute error, d) relative bias, e)
485 Nash-Sutcliffe efficiency coefficient, f) probability of detection, g) false alarm ratio, and h) critical success index.

486 **4.3 Model performance on rain events predictions**

487 To measure the WHU-SGCC performance on predicting rain events, daily precipitation thresholds of 0.1, 10, 25, and 50 mm

488 were considered, and the results are shown in Table 5 and Table 6. The average percentage of each class of rain events at the

validation gauge station during the four seasons from 1990 to 2014 are shown in Table 5. The major rain events within the Jinsha River Basin were no rain (<0.1 mm) and light rain (0.1-10 mm), which accounted for more than 80% of the total days (the average percentage of rain event days of the total days at each gauge station), while the number of days with daily precipitation greater than the 50 mm was the smallest (no more than 1% of the total days) and fewer than 5% of the days had daily precipitation in the range of 25 mm to 50 mm. In the spring, fall and summer, significantly more no-rain days occurred than rainy days, and approximately 5% of the days had daily precipitation of 10-50 mm. The seasonal distribution of rainfall was concentrated in the summer, and 54.76%, 14.01% and 3.62% of the days had daily precipitation of 0.1-10, 10-25, and 25-50 mm, respectively. The results indicated that the average daily precipitation was less than 10 mm throughout the years of the study.

Table 5 The average percentage of each class of rain events at the validation gauge station during the four seasons from 1990 to 2014 within the Jinsha River Basin.

Rain event (mm) / Season	<0.1	[0.1,10)	[10,25)	[25,50)	>=50
Spring	57.87%	38.43%	3.29%	0.39%	0.02%
Summer	26.89%	54.76%	14.01%	3.62%	0.72%
Fall	57.32%	36.62%	4.99%	0.93%	0.14%
Winter	85.78%	13.99%	0.21%	0.01%	0.00%

The WHU-SGCC approach had lower errors than CHIRP and CHIRPS, as indicated by the RMSE, MAE and BIAS, but the performance of WHU-SGCC is not promising for events with total rainfall greater than 25 mm in the summer (Fig. 8). This negative performance for total rainfall higher than 25 mm in the summer might be attributed to the overestimation of rainfall by CHIRP and CHIRPS. For the seasonal distribution of precipitation (Table 5), the average daily precipitation within the basin less than 10 mm over the study period, which results in numerous rain gauge station data with values lower than 10 mm, which had a significant impact on the establishment of statistical relationships for the WHU-SGCC. The estimates of extreme rain events might also be attenuated during the process of WHU-SGCC adjustment.

Besides, the POD and CSI results of CHIRPS are the worst, while the results of the WHU-SGCC are the highest, which indicate its superiority for the detection of precipitation events. As for the results of the WHU-SGCC, the assessments of POD and CSI are the best in the summer, followed by the fall, spring, and winter, which are related to the seasonal rainfall pattern of more rain in the summer and less in the winter.

Therefore, the WHU-SGCC approach is applicable for the detection of rainfall events in the Jinsha River Basin, while in the summer it is better with rainfall less than or approximately equal to the average daily precipitation. Due to the homogenization of the WHU-SGCC method, its performance for short intense and extreme rain events was poorer than those of CHIRP and CHIRPS, which should be improved in a future study.
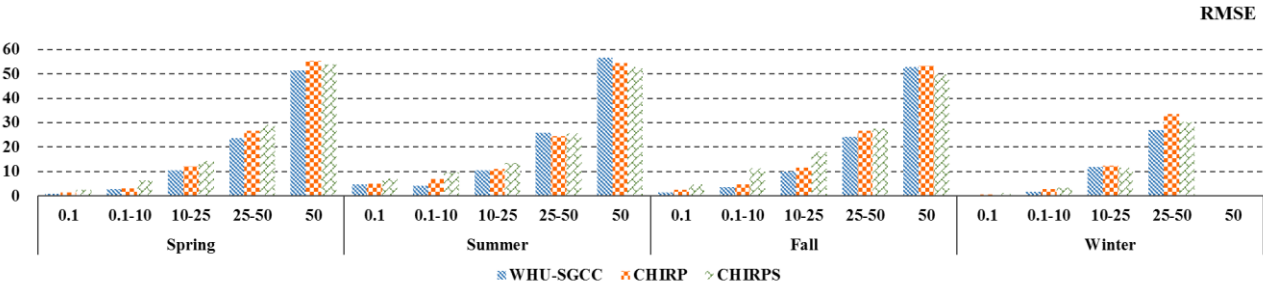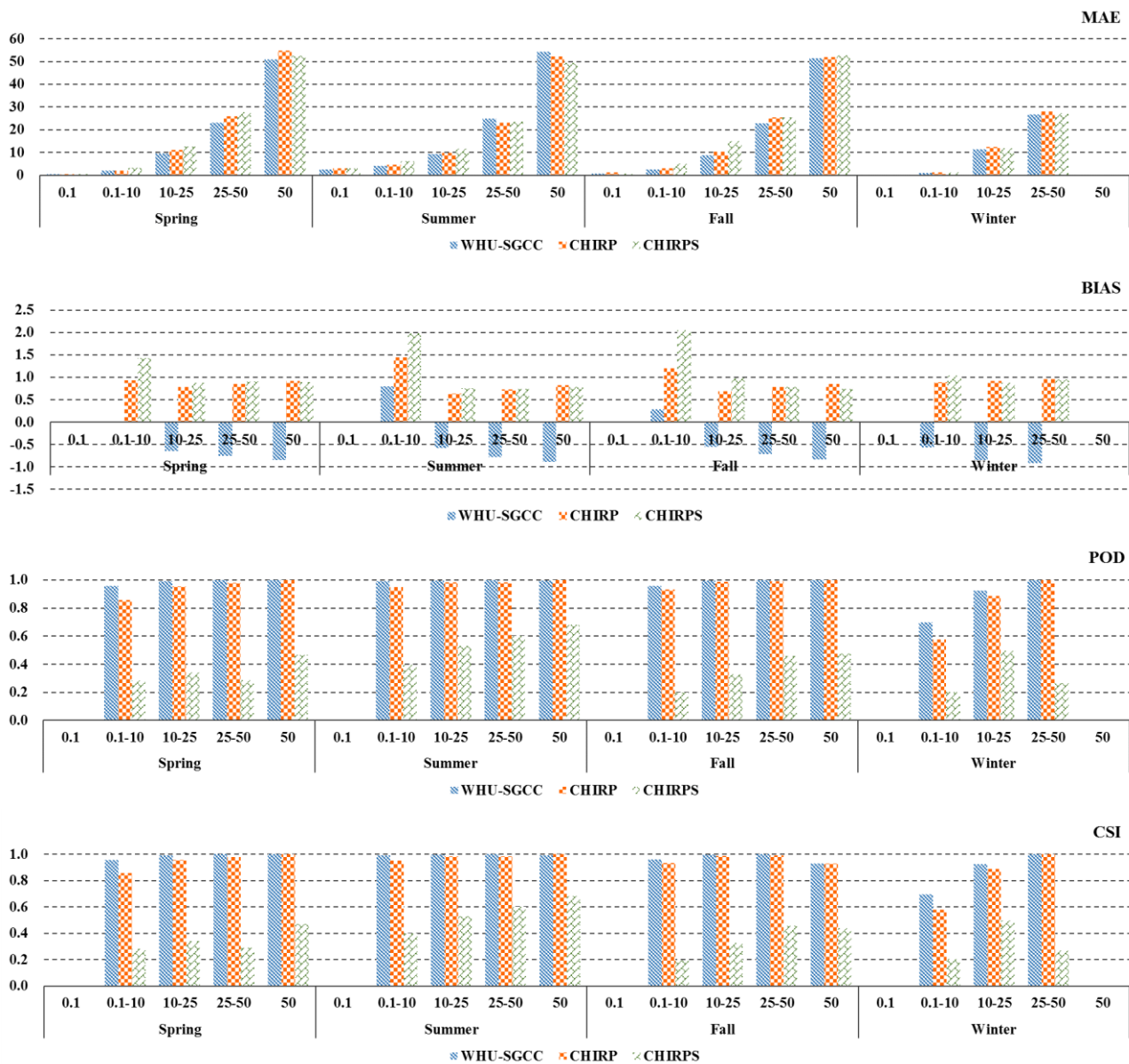
Figure 8 Accuracy assessment of liquid precipitation events from 1990 to 2014.

5 Data availability

All the resulting dataset derived from the WHU-SGCC approach is available on PANGAEA, with the following DOI: https://doi.pangaea.de/10.1594/PANGAEA.900620 (Shen et al., 2019). The high-resolution (0.05°) daily precipitation estimation data over the Jinsha River Basin from 1990 to 2014 can be downloaded in TIFF format.

6 Conclusions

This study provides a novel approach, the WHU-SGCC method, for merging daily satellite-based precipitation estimates with observations. A case study of the Jinsha River Basin was conducted to verify the effectiveness of the WHU-SGCC approach during all four seasons from 1990 to 2014, and the adjusted precipitation estimates were compared to CHIRP and CHIRPS. The WHU-SGCC method aims to reduce the errors and uncertainties in CHIRP data over regions with complicated mountainous terrain and sparse rain gauges. To the best of the authors' knowledge, this study is the first to use daily CHIRP and CHIRPS data in this area.

According to our findings, the following conclusions can be drawn: (1) The WHU-SGCC method is effective for the

adjustment of precipitation biases from points to surfaces. The precipitation adjusted by the WHU-SGCC method can achieve greater accuracy compared with CHIRP and CHIRPS, with average improvements of Pearson's correlation coefficient (PCC) of 0.01-0.23 and 0.06-0.32, respectively. The PCCs were improved to more than 0.5 in the spring and fall and to approximately 0.5 in the winter, and they were the worst in the summer, which may be attributed to the greater precipitation in the summer and lower precipitation in the winter. In addition, the NSE of the WHU-SGCC provides substantial improvements over CHIRP and CHIRPS, which reached 0.2836, 0.2944 and 0.1853 in the spring, fall and winter, respectively. In the summer, the NSE of the WHU-SGCC is still negative, but it is improved to be nearly zero, which indicates that the adjusted results are similar to the average level of the rain gauge observations. All of the measured errors were reduced except for the BIAS, which showed no significant improvement in the summer but was approximately 0. Overall, the WHU-SGCC approach achieves good performance in error correction of CHIRP and CHIRPS. (2) The spatial distribution of the precipitation estimate accuracy derived from the WHU-SGCC method is related to the topographic complexity. These errors over the lower elevation regions and the large size of light precipitation events with short durations resulted in a limited improvement in accuracy, with PCC values less than 0.3. However, higher PCCs and lower errors were observed over the north-central part of the river basin, which is a drier region with complex terrain and sparse rain gauges. The spatial distribution statistics indicate that the WHU-SGCC method is promising for the adjustment of satellite biases by blending with the observations over regions of complex terrain. (3) The leave-one-out cross validation of WHU-SGCC on daily rain events confirmed that the model is effective in the detection of precipitation events that are less than or approximately equal to the average annual precipitation in the Jinsha River Basin.The WHU-SGCC approach achieves reductions of the RMSE, MAE and BIAS metrics, while on rain events less than 25 mm in the summer. Specifically, the WHU-SGCC has the best ability to reduce precipitation errors for daily accuracy evaluations, with average reductions of 15% and 34% for compared to CHIRP and CHIRPS, respectively. In spite of the corrections, the uncertainties in the precipitation forecasts in the summer are still large, which may due to the homogenization attenuating the simulation of extreme rain events.

In conclusion, the WHU-SGCC approach can help adjust the biases of daily satellite-based precipitation estimates over the Jinsha River Basin, which contains complicated mountainous terrain with sparse rain gauges. This approach is a promising tool to monitor daily precipitation over the Jinsha River Basin, considering the spatial correlation and historical precipitation characteristics between raster pixels in regions with similar topographic features. Future development of the WHU-SGCC approach will focus on the following three aspects: (1) the improvement of the adjusted precipitation quality to better monitor extreme rainfall events by blending multiple data sources for different rain events; (2) the introduction of more climatic factors and multi-model ensembles to achieve more accurate spatial distributions of precipitation; and (3) investigations of the performance over other areas and for particular hydrological cases to validate the applicability of WHU-SGCC approach.

Appendix A: Geographical characteristics of rain stations

The station identification numbers and relevant geographical characteristics are shown in Table A1.

Table A1 Geographical characteristics of the rain stations.

Station number	Province	Lat (°N)	Lon (°E)	Elevation (m)
52908	Qinghai	35.13	93.05	4823
56004	Qinghai	34.13	92.26	4744
56021	Qinghai	34.07	95.48	5049
56029	Qinghai	33.00	96.58	4510
56034	Qinghai	33.48	97.08	4503
56144	Tibet	31.48	98.35	4743
56038	Sichuan	32.59	98.06	4285
56146	Sichuan	31.37	100.00	4703
56152	Sichuan	32.17	100.20	4401
56167	Sichuan	30.59	101.07	3374
56247	Sichuan	30.00	99.06	2948

56251	Sichuan	30.56	100.19	4284
56257	Sichuan	30.00	100.16	3971
56357	Sichuan	29.03	100.18	4280
56374	Sichuan	30.03	101.58	3902
56459	Sichuan	27.56	101.16	3002
56462	Sichuan	29.00	101.30	4019
56475	Sichuan	28.39	102.31	1850
56479	Sichuan	28.00	102.51	2470
56485	Sichuan	28.16	103.35	2060
56565	Sichuan	27.26	101.31	2578
56571	Sichuan	27.54	102.16	1503
56666	Sichuan	26.35	101.43	1567
56671	Sichuan	26.39	102.15	1125
56543	Yunnan	27.50	99.42	3216
56586	Yunnan	27.21	103.43	2349
56651	Yunnan	26.51	100.13	2449
56664	Yunnan	26.38	101.16	1540
56684	Yunnan	26.24	103.15	2184
56778	Yunnan	25.00	102.39	1975

566 **Appendix B: Multi-year land cover type**

567 The multi-year land cover types in the Jinsha River Basin from 2001 to 2013 are shown in Fig. B1. All of the land cover type

568 maps were derived from the MODIS/Terra+Aqua Land Cover Type Yearly L3 Global 500 m SIN Grid V051 data set, which

569 is available online at https://search.earthdata.nasa.gov/search/granules?p=C200106111-

570 LPDAAC_ECS&q=MCD12&ok=MCD12 (last access: 23 July 2019). Fig. B1 shows that the land use had no obvious changes

571 over the study period. In addition, the upstream area of the Jinsha River is an untraversed region that has not been affected

572 significantly by human activities. Thus, the land use in the study area has hardly changed.

573

574

575

576

577
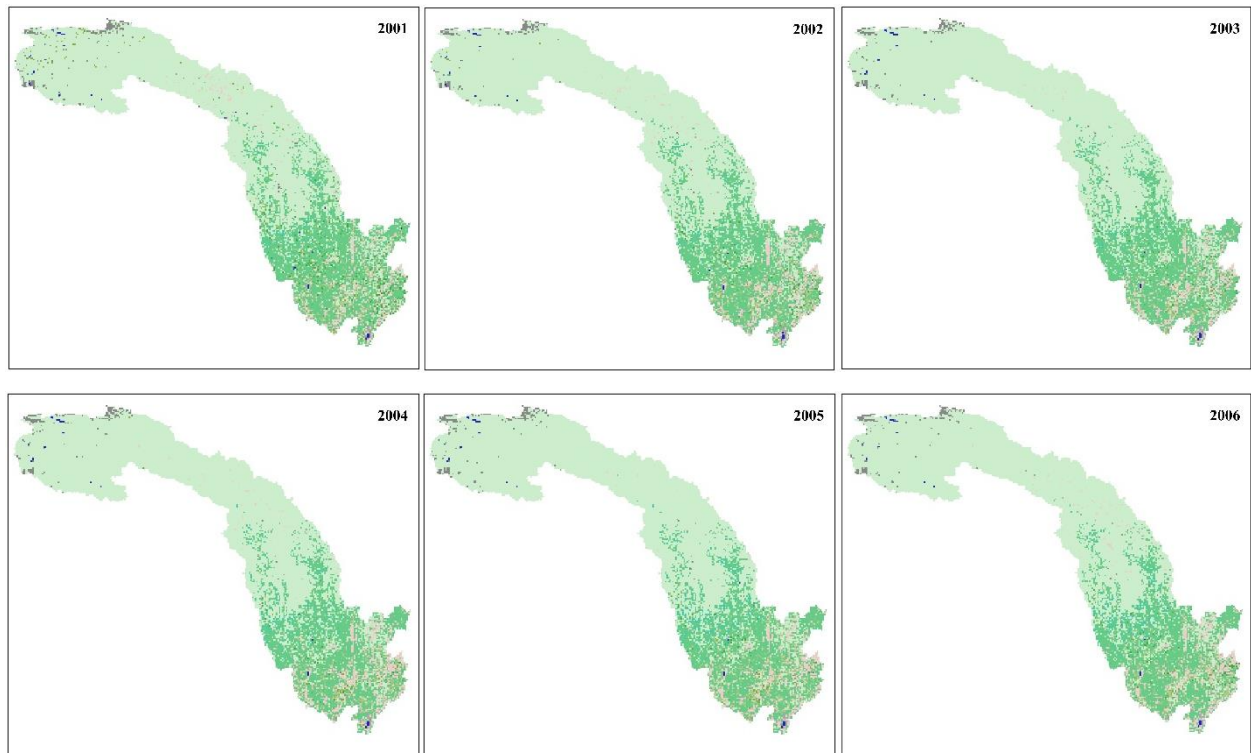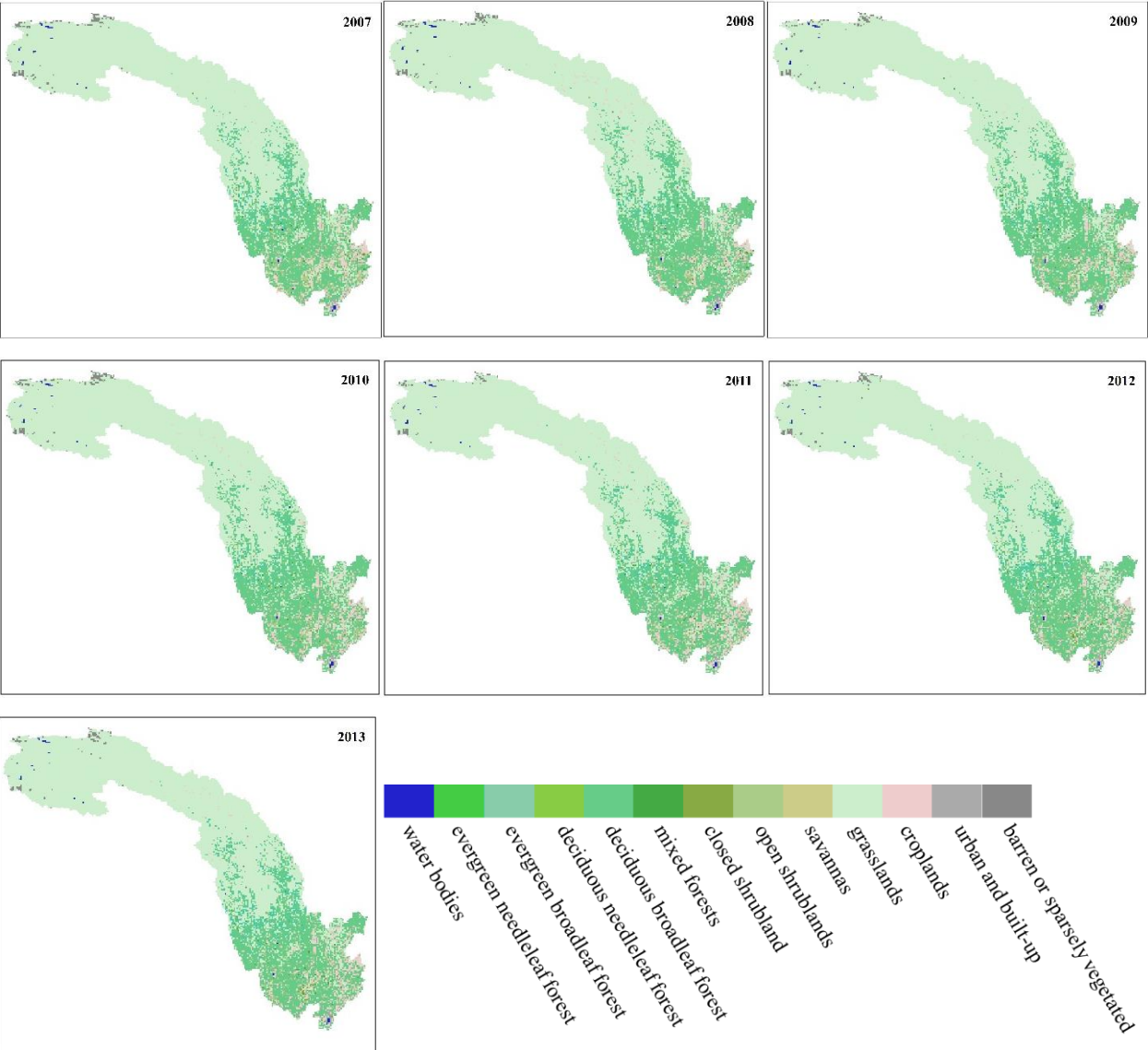
578 **Figure B1** Land cover types over the Jinsha River Basin from 2001 to 2013.

579 **Appendix C: Selection of decision trees for random forest regression**

52908

56004
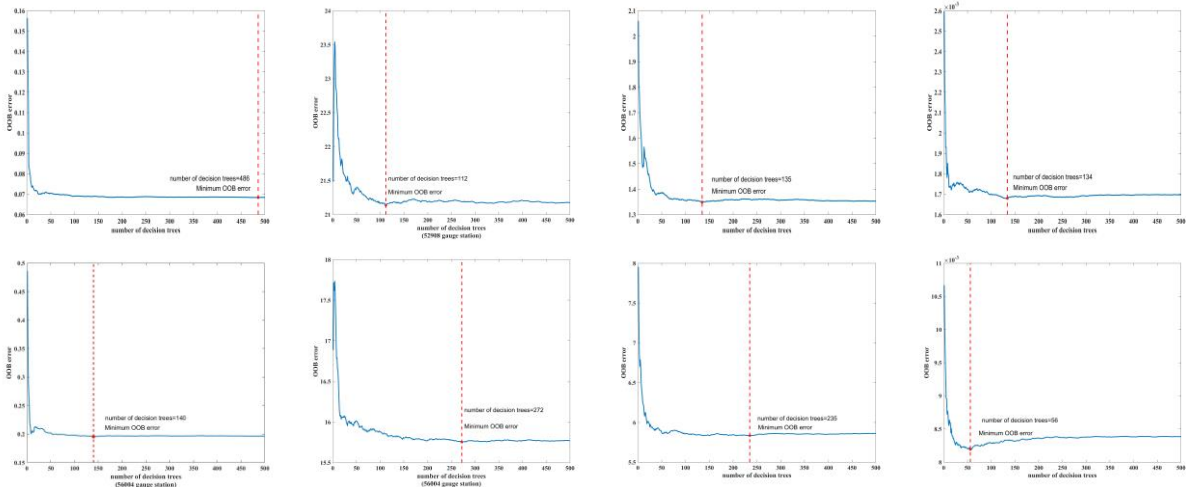
56021
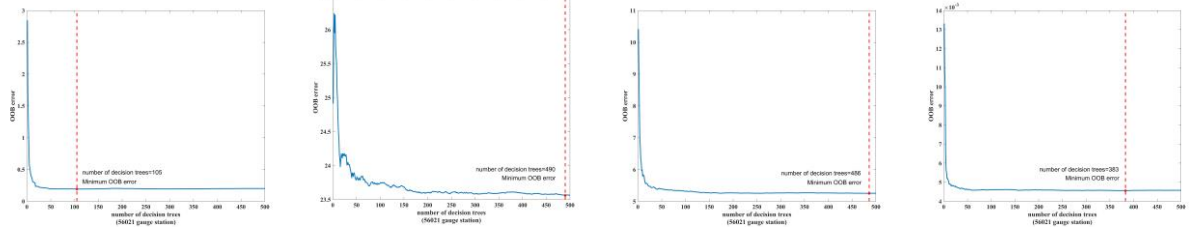
56029
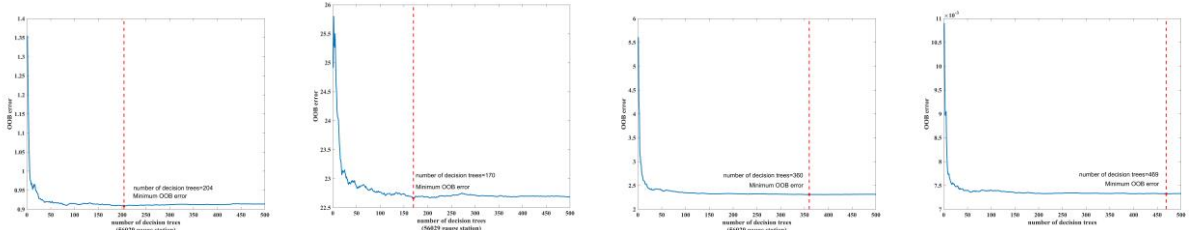
56374
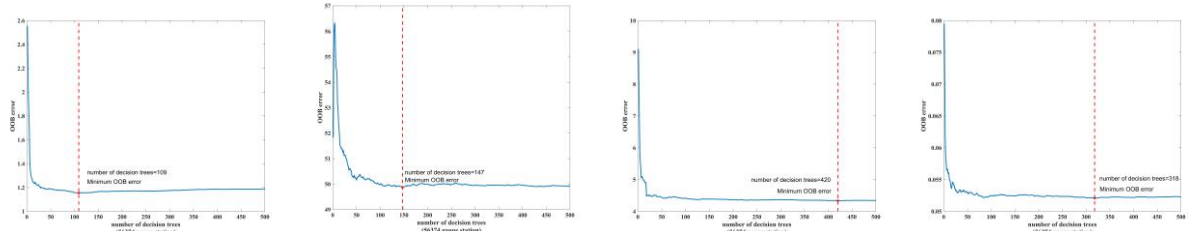
56459
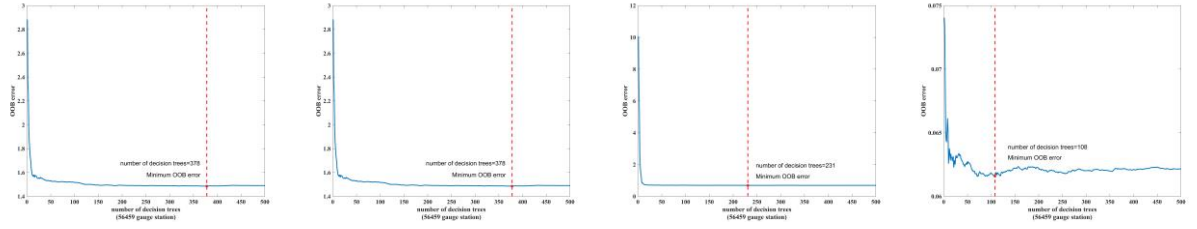
56462
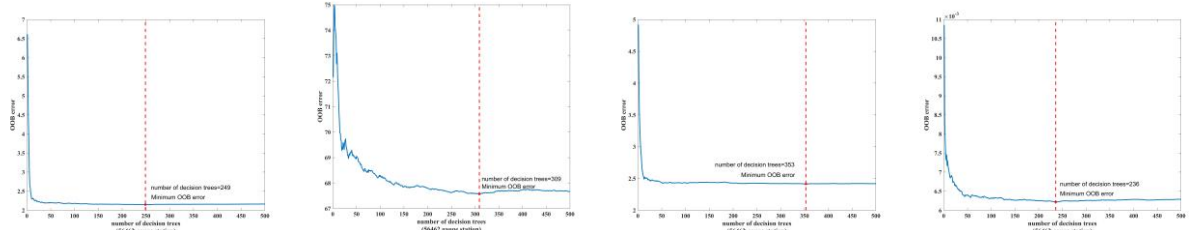
56475
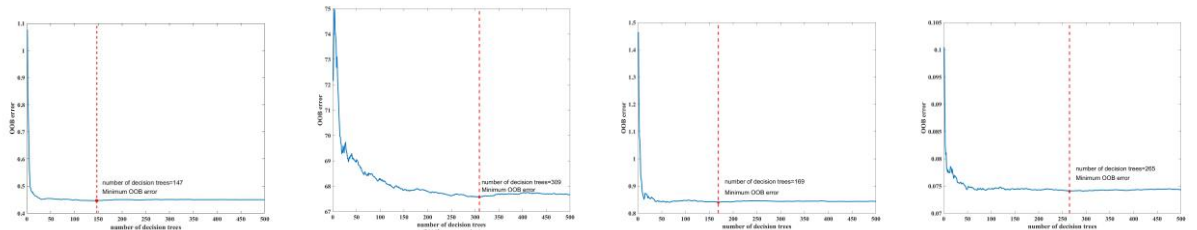
56479
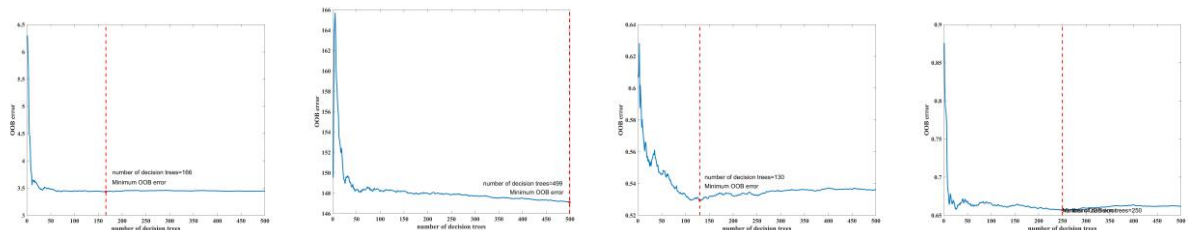
56485
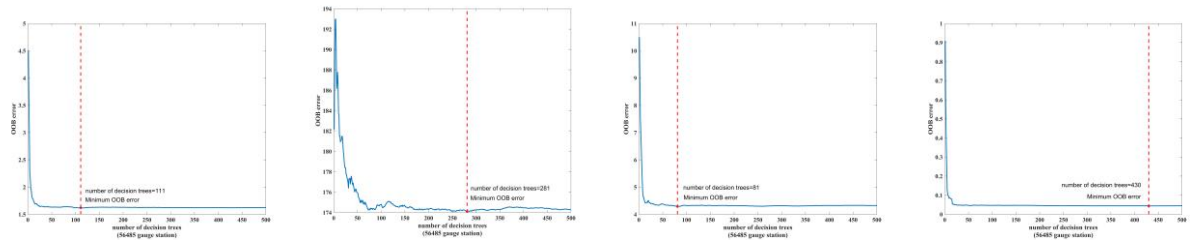
56543
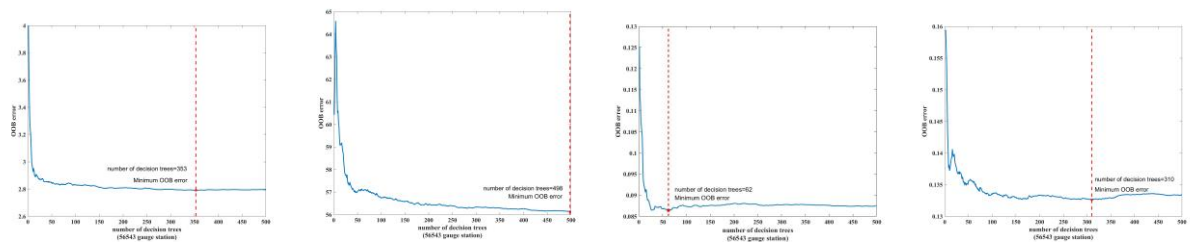
56565
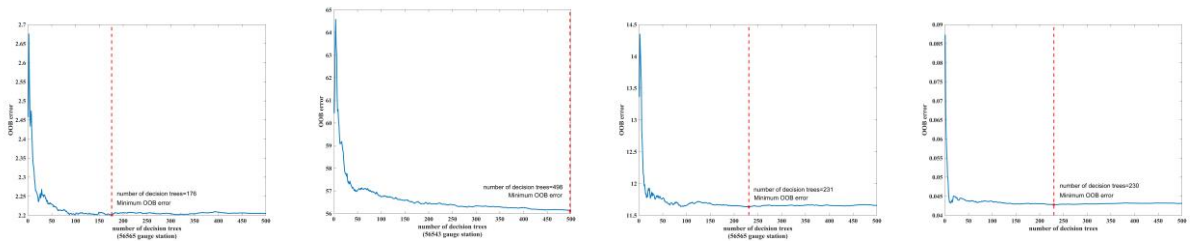
56571
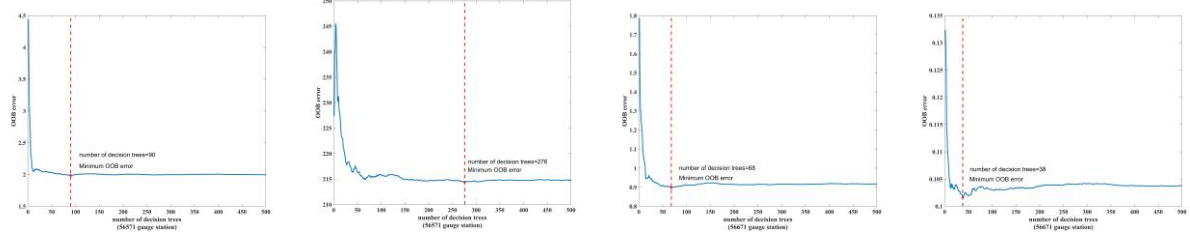
56684
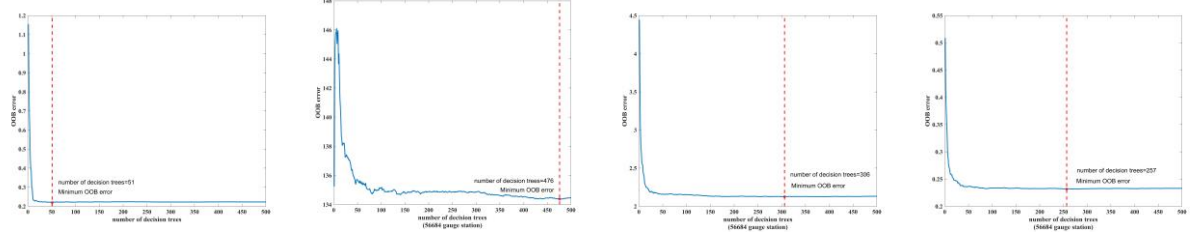
56778
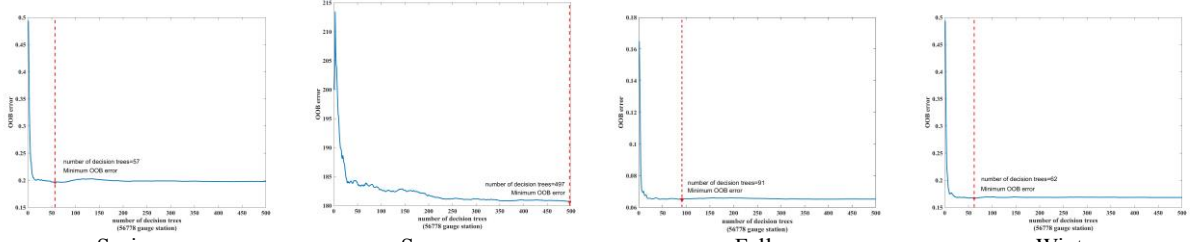
Spring	Summer	Fall	Winter

Figure C1 Changes in the out-of-bag (OOB) error with increasing number of decision trees by means of random forest regression at each gauge station.

Appendix D: Spatial distribution of C1, C2 and C3 pixels

591

Validation gauge station	Pixel type Spring	Summer	Fall	Winter
52908	C4	C4	C4	C4
56004	C4	C4	C4	C4
56021	C2	C2	C2	C3
56029	C2	C3	C2	C3
56034	C2	C3	C2	C3
56038	C4	C4	C4	C4
56144	C4	C4	C4	C4
56146	C4	C4	C4	C4
56152	C2	C3	C3	C4
56167	C4	C2	C2	C4
56247	C4	C4	C4	C4
56251	C2	C2	C3	C3
56257	C4	C4	C4	C4
56357	C4	C4	C4	C4
56374	C4	C4	C3	C4
56459	C4	C4	C4	C4
56462	C4	C4	C4	C4
56475	C4	C3	C3	C3
56479	C4	C4	C4	C4
56485	C3	C2	C2	C3
56543	C3	C3	C4	C4
56565	C2	C2	C3	C3
56571	C2	C4	C4	C4
56586	C2	C3	C2	C3
56651	C3	C2	C2	C3
56664	C4	C4	C4	C4
56666	C3	C3	C3	C3
56671	C3	C2	C2	C3
56684	C2	C2	C2	C4
56778	C4	C3	C3	C4

Table D1 Pixel type of the validation gauge station.

592
593

52908
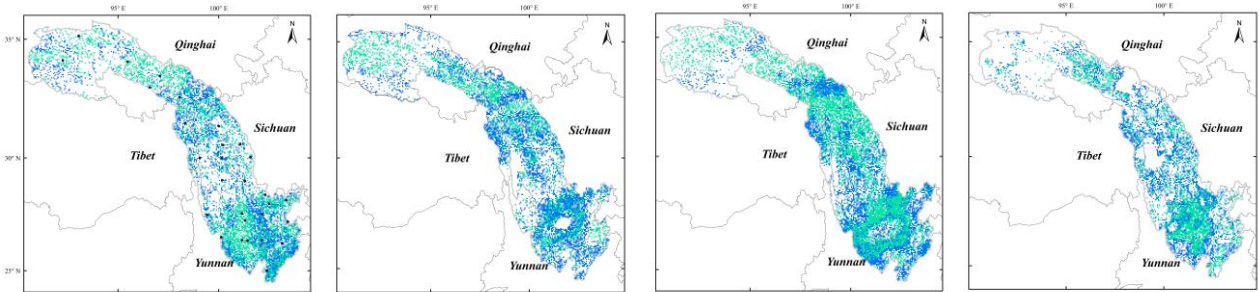
56004
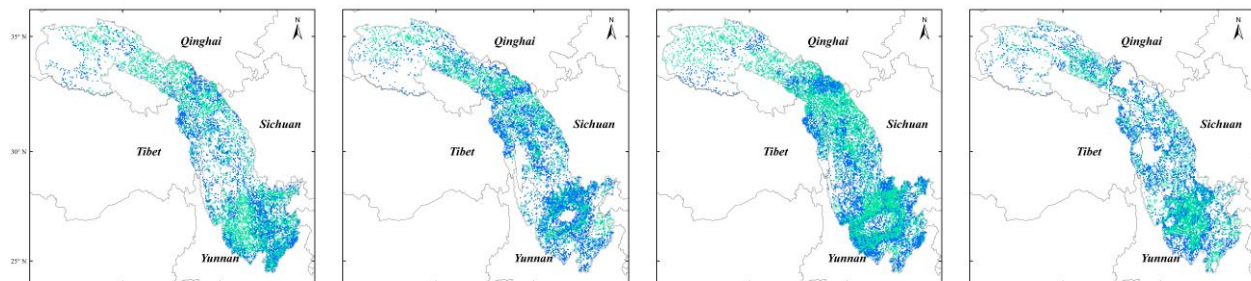
56021
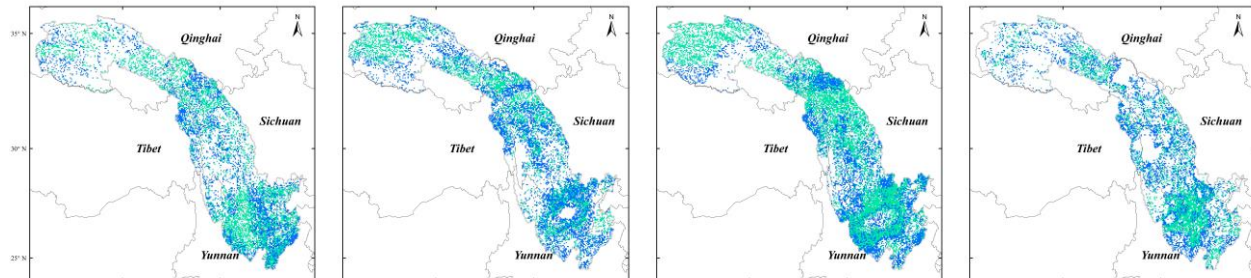
56029
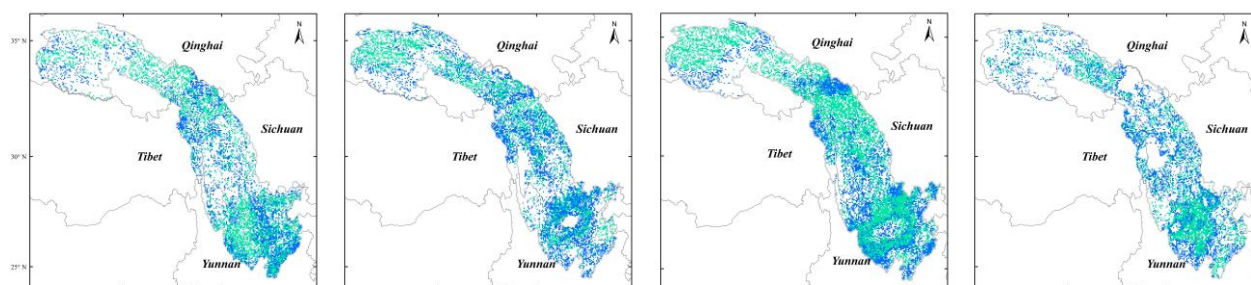
56034
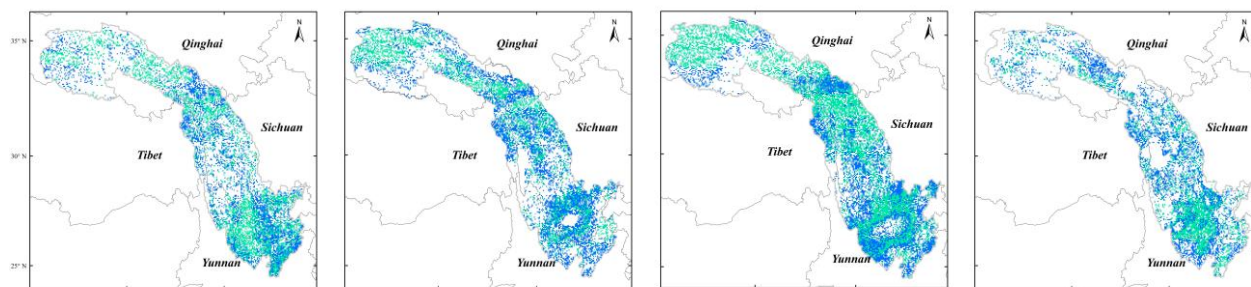
56038
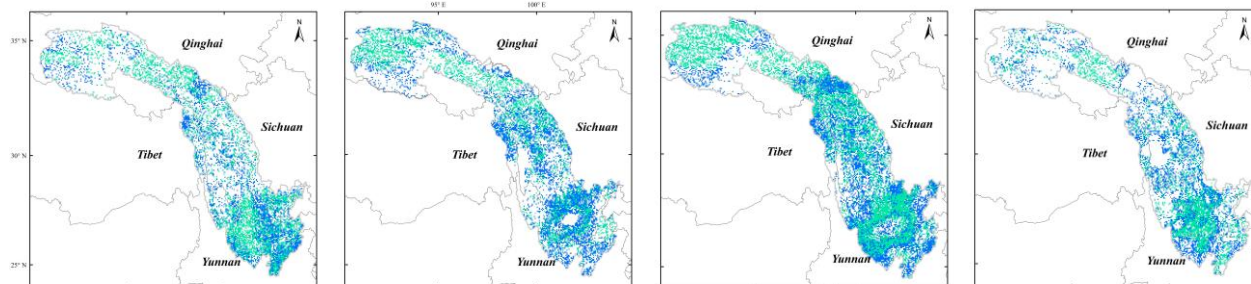
56144
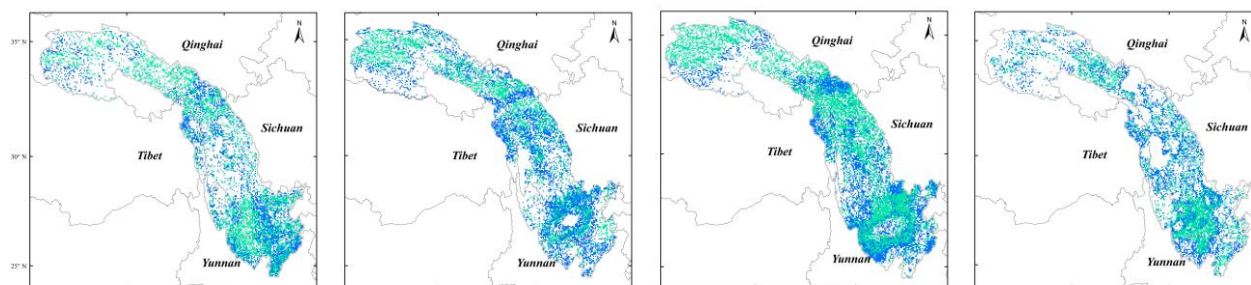
56146
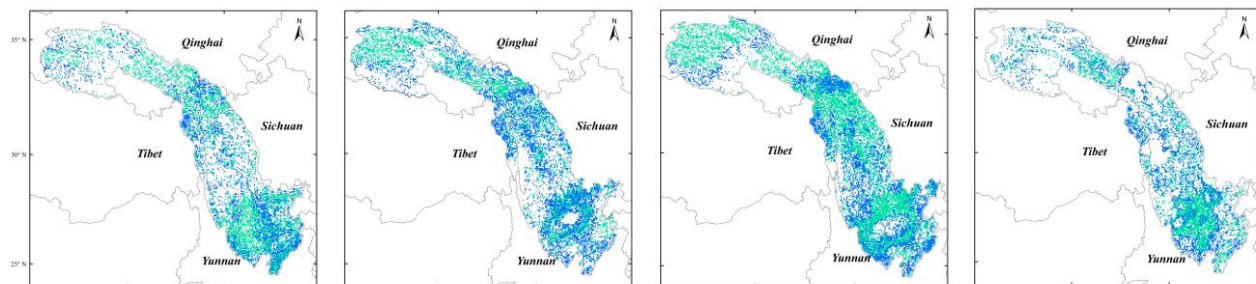
56152
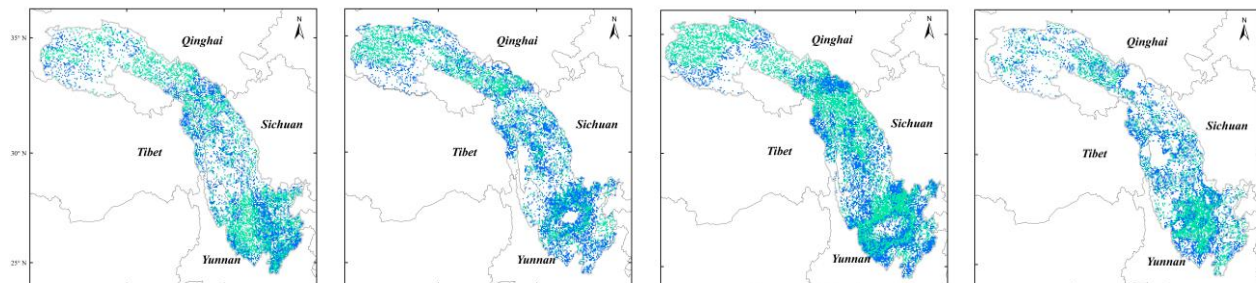
56167
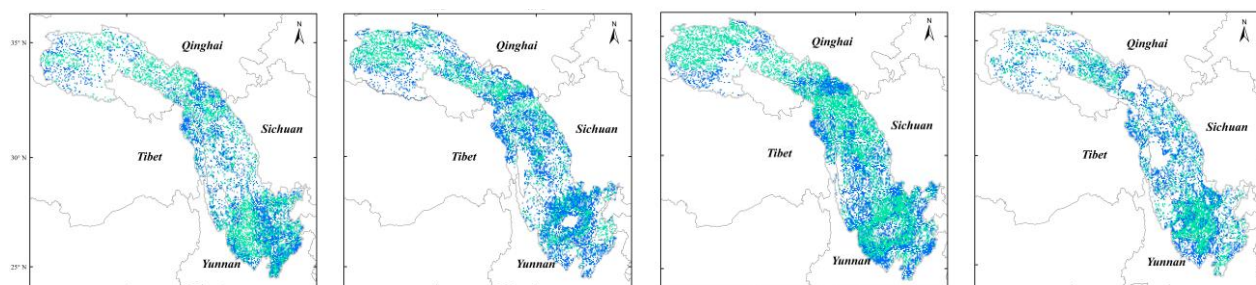
56247
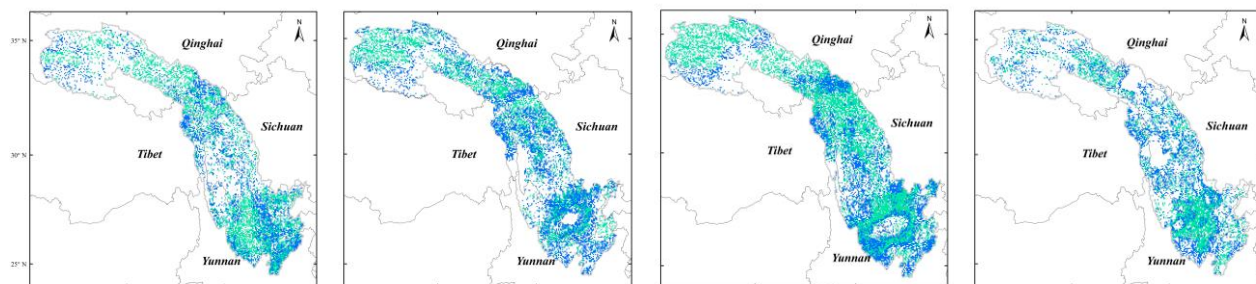
56251
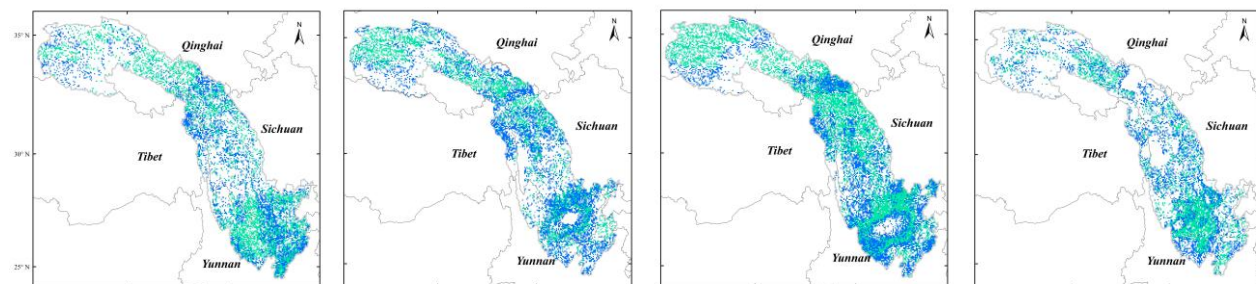
56257
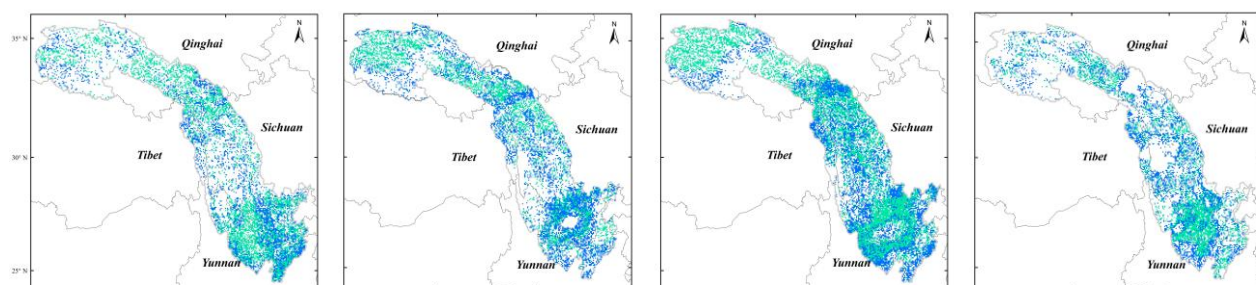
56357

56374

56459

56462

56475

56479

594
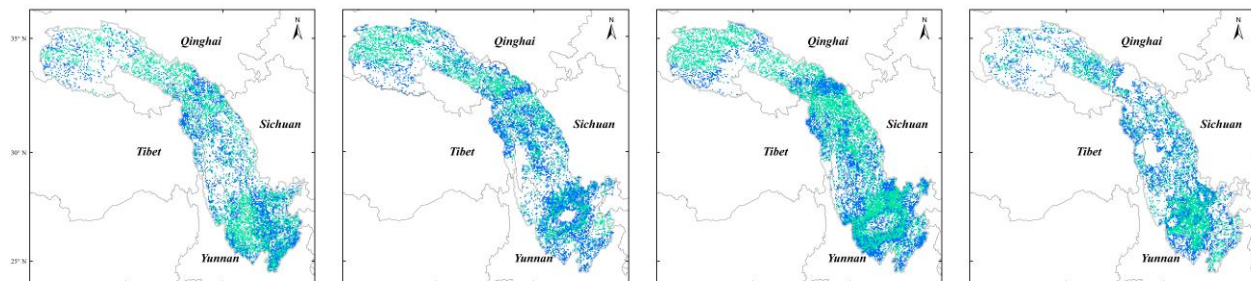
595
596 **Figure D1** Spatial distribution of each class of pixels adjusted by each rule using the WHU-SGCC method in the Jinsha River Basin.

597

598 **Appendix E: Spatial Clustering from the FCM method**

599
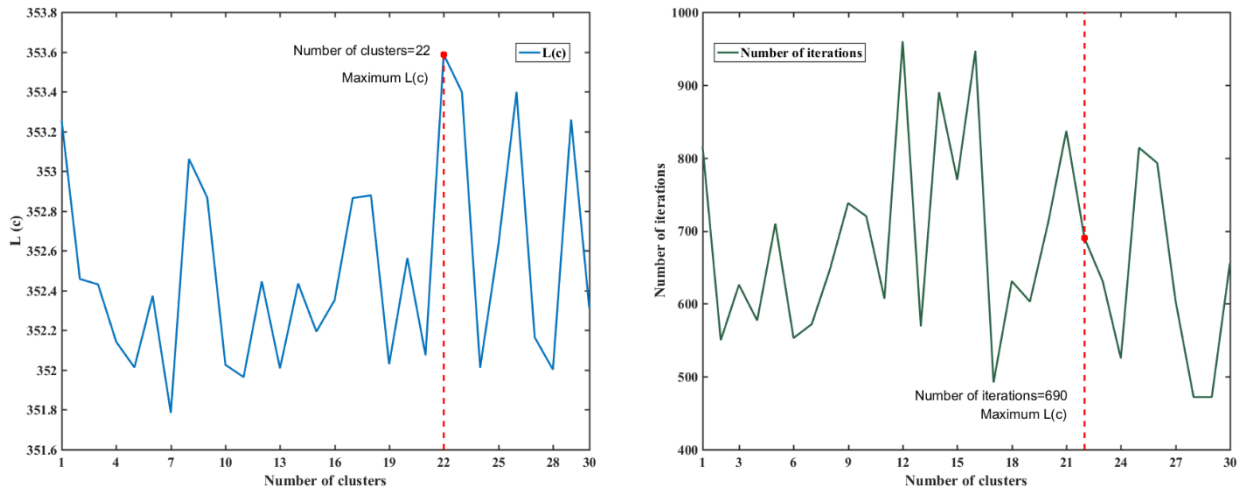
600 **Figure E1** Optimum number of clusters determined by the maximum $L(c)$ with the iterative process.

601
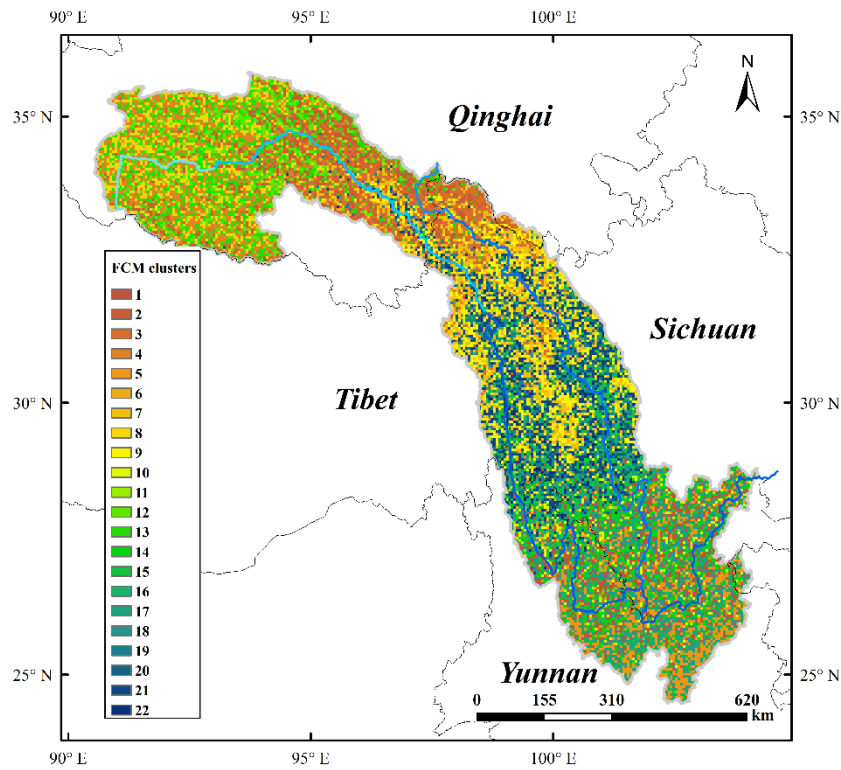
602 **Figure E2** Spatial clustering as defined by the FCM method in the Jinsha River Basin.

603 This appendix shows how to set the number of clusters in the FCM method.

604   To adjust the pixels other than those of the gauge stations, the pixels that are statistically similar to the C1 pixels were

605 selected. According to Rule 2, the C2 pixels were identified in a spatial area defined by the FCM method. In the following

606 experiments of Rule 2, we set the parameters $m = 2, \varepsilon = 0.00001$, and the maximum number of iterations was set 1000 (a

607 sufficiently large value considering the algorithm efficiency). To determine the optimal numbers of clusters, the value of c was

608 varied from 1 to 30 with an increment of 1.The values of $L(c)$ during the running of the FCM are shown in Fig E1. The optimum

609 number of clusters was 22, and the number of iterations was 690 less than the maximum number of iterations.

610   Therefore, the number of clusters was set to 22, and the number of iterations was set to 1000 for full operation by means of

611 the FCM. The spatial clustering results considering the terrain factors are shown in Fig. E2. In general, the spatial results of

612 the FCM have many of the same characteristics as the areas defined by the terrain variations, especially with respect to the

613 slope and runoff directions, which may influence the regional rainfall.

7 Acknowledgments

This work was supported by the National Natural Science Foundation of China program (no. 41771422), the Nature Science Foundation of Hubei Province (no. 2017CFB616), the fundamental research funds for the central universities (no. 2042017kf0211), and the LIESMARS Special Research Funding.

The authors would like to thank data support: the Climate Hazards Group at the University of California, Santa Barbara, for providing CHIRP and CHIRPS datasets (http://chg.ucsb.edu/data/), and the National Climate Center (NCC) of the China Meteorological Administration (CMA) for providing the daily rain gauged observations and gridded precipitation observations (http://data.cma.cn/). The authors also thank the PANGAEA Data Publisher for Earth & Environmental Science platform for providing the storage to disseminate the data generated in this experiment.

The authors are grateful for the editor and anonymous reviewers for their useful suggestions that clearly improved this paper.

References

AghaKouchak, A., Behrangi, A., Sorooshian, S., Hsu, K., and Amitai, E.: Evaluation of satellite-retrieved extreme precipitation rates across the central United States, J. Geophys. Res.-Atmos., 116, 11, doi:10.1029/2010jd014741, 2011.

Agutu, N. O., Awange, J. L., Zerihun, A., Ndehedehe, C. E., Kuhn, M., and Fukuda, Y.: Assessing multi-satellite remote sensing, reanalysis, and land surface models' products in characterizing agricultural drought in East Africa, Remote Sens. Environ., 194, 287-302, doi:10.1016/j.rse.2017.03.041, 2017.

Ali, H., and Mishra, V.: Contrasting response of rainfall extremes to increase in surface air and dewpoint temperatures at urban locations in India, Sci Rep, 7, 1228, doi:10.1038/s41598-017-01306-1, 2017.

Anders, A. M., Roe, G. H., Hallet, B., Montgomery, D. R., Finnegan, N. J., and Putkonen, J.: Spatial patterns of precipitation and topography in the Himalaya, Tectonics, Climate, and Landscape Evolution, 398, 39-53, doi:10.1130/2006.2398(03), 2006.

Aonashi, K., Awaka, J., Hirose, M., Kozu, T., Kubota, T., Liu, G., Shige, S., Kida, S., Seto, S., Takahashi, N., and Takayabu, Y. N.: GSMaP Passive Microwave Precipitation Retrieval Algorithm : Algorithm Description and Validation, Journal of the Meteorological Society of Japan, 87A, 119-136, 10.2151/jmsj.87A.119, 2009.

Ashouri, H., Hsu, K.-L., Sorooshian, S., Braithwaite, D. K., Knapp, K. R., Cecil, L. D., Nelson, B. R., and Prat, O. P.: PERSIANN-CDR: Daily Precipitation Climate Data Record from Multisatellite Observations for Hydrological and Climate Studies, Bulletin of the American Meteorological Society, 96, 69-83, doi:10.1175/bams-d-13-00068.1, 2015.

Bai, L., Shi, C. X., Li, L. H., Yang, Y. F., and Wu, J.: Accuracy of CHIRPS Satellite-Rainfall Products over Mainland China, Remote Sens., 10, 28, doi:10.3390/rs10030362, 2018.

Beck, H. E., Vergopolan, N., Pan, M., Levizzani, V., van Dijk, A. I. J. M., Weedon, G. P., Brocca, L., Pappenberger, F., Huffman, G. J., and Wood, E. F.: Global-scale evaluation of 22 precipitation datasets using gauge observations and hydrological modeling, Hydrology and Earth System Sciences, 21, 6201-6217, 10.5194/hess-21-6201-2017, 2017.

Beck, H. E., Wood, E. F., Pan, M., Fisher, C. K., Miralles, D. G., van Dijk, A. I. J. M., McVicar, T. R., and Adler, R. F.: MSWEP V2 Global 3-Hourly 0.1 degrees Precipitation: Methodology and Quantitative Assessment, Bulletin of the American Meteorological Society, 100, 473-502, 10.1175/bams-d-17-0138.1, 2019.

Behrangi, A., Andreadis, K., Fisher, J. B., Turk, F. J., Granger, S., Painter, T., and Das, N.: Satellite-Based Precipitation Estimation and Its Application for Streamflow Prediction over Mountainous Western US Basins, J. Appl. Meteorol. Climatol., 53, 2823-2842, doi:10.1175/jamc-d-14-0056.1, 2014.

Berndt, C., Rabiei, E., and Haberlandt, U.: Geostatistical merging of rain gauge and radar data for high temporal resolutions and various station density scenarios, Journal of Hydrology, 508, 88-101, doi:10.1016/j.jhydrol.2013.10.028, 2014.

Cattani, E., Merino, A., Guijarro, J. A., and Levizzani, V.: East Africa Rainfall Trends and Variability 1983-2015 Using Three

655   Long-Term Satellite Products, Remote Sens., 10, 26, doi:10.3390/rs10060931, 2018.

656 Chen, F. W., and Liu, C. W.: Estimation of the spatial rainfall distribution using inverse distance weighting (IDW) in the middle

657   of Taiwan, Paddy Water Environ., 10, 209-222, 10.1007/s10333-012-0319-1, 2012.

658 Chen, J., Brissette, F. P., Chaumont, D., and Braun, M.: Finding appropriate bias correction methods in downscaling

659   precipitation for hydrologic impact studies over North America, Water Resources Research, 49, 4187-4205,

660   doi:10.1002/wrcr.20331, 2013.

661 Derin, Y., Anagnostou, E., Berne, A., Borga, M., Boudevillain, B., Buytaert, W., Chang, C.-H., Delrieu, G., Hong, Y., Hsu, Y.

662   C., Lavado-Casimiro, W., Manz, B., Moges, S., Nikolopoulos, E. I., Sahlu, D., Salerno, F., Rodriguez-Sanchez, J.-P.,

663   Vergara, H. J., and Yilmaz, K. K.: Multiregional Satellite Precipitation Products Evaluation over Complex Terrain, J.

664   Hydrometeorol., 17, 1817-1836, 10.1175/jhm-d-15-0197.1, 2016.

665 Duan, Z., Liu, J. Z., Tuo, Y., Chiogna, G., and Disse, M.: Evaluation of eight high spatial resolution gridded precipitation

666   products in Adige Basin (Italy) at multiple temporal and spatial scales, Sci. Total Environ., 573, 1536-1553,

667   doi:10.1016/j.scitotenv.2016.08.213, 2016.

668 Dunn, J. C.: A fuzzy relative of the ISODATA Process and Its Use in Detecting Compact Well-Separated Clusters, Journal of

669   Cybernetics, 3, 32-57, 1973.

670 Durre, I., Menne, M. J., Gleason, B. E., Houston, T. G., and Vose, R. S.: Comprehensive Automated Quality Assurance of

671   Daily Surface Observations, J. Appl. Meteorol. Climatol., 49, 1615-1633, doi:10.1175/2010jamc2375.1, 2010.

672 Funk, C., Peterson, P., Landsfeld, M., Pedreros, D., Verdin, J., Shukla, S., Husak, G., Rowland, J., Harrison, L., Hoell, A., and

673   Michaelsen, J.: The climate hazards infrared precipitation with stations-a new environmental record for monitoring

674   extremes, Sci. Data, 2, 21, doi:10.1038/sdata.2015.66, 2015 a.

675 Funk, C., Verdin, A., Michaelsen, J., Peterson, P., Pedreros, D., and Husak, G.: A global satellite-assisted precipitation

676   climatology, Earth Syst. Sci. Data, 7, 275-287, 10.5194/essd-7-275-2015, 2015 b.

677 Funk, C., Peterson, P., Landsfeld, M., Pedreros, D., Verdin, J., Rowland, J., Bo, E., Husak, G. J., Michaelsen, J. C., and Verdin,

678   A. P.: A Quasi-Global Precipitation Time Series for Drought Monitoring Data Series 832, Usgs Professional Paper, Data

679   Series, 2014.

680 Genuer, R., Poggi, J. M., Tuleau-Malot, C., and Villa-Vialaneix, N.: Random Forests for Big Data, Big Data Res., 9, 28-46,

681   doi:10.1016/j.bdr.2017.07.003, 2017.

682 Hou, A. Y., Kakar, R. K., Neeck, S., Azarbarzin, A. A., Kummerow, C. D., Kojima, M., Oki, R., Nakamura, K., and Iguchi, T.:

683   The Global Precipitation Measurement Mission, Bulletin of the American Meteorological Society, 95, 701-722,

684   10.1175/bams-d-13-00164.1, 2014.

685 Huffman, G. J., Adler, R. F., Bolvin, D. T., Gu, G., Nelkin, E. J., Bowman, K. P., Hong, Y., Stocker, E. F., and Wolff, D. B.:

686   The TRMM multisatellite precipitation analysis (TMPA): Quasi-global, multiyear, combined-sensor precipitation

687   estimates at fine scales, J. Hydrometeorol., 8, 38-55, 10.1175/jhm560.1, 2007.

688 Huffman, G. J., Adler, R. F., Bolvin, D. T., and Nelkin, E. J.: The TRMM Multi-Satellite Precipitation Analysis (TMPA), in:

689   Satellite Rainfall Applications for Surface Hydrology, edited by: Gebremichael, M., and Hossain, F., Springer Netherlands,

690   Dordrecht, 3-22, 2010.

691 Huffman, G. J, D. T. Bolvin, D. Braithwaite, K. Hsu, R. Joyce, P. Xie.: NASA Global Precipitation Measurement Integrated

692   Multi-satellitE Retrievals for GPM (IMERG), NASA Algorithm theoretical basis document (ATBD) version 5.2., 35 pp.

693   https://pmm.nasa.gov/sites/default/files/document_files/IMERG_ATBD_V5.2.pdf, 2018.

694 Johnson, R. W.: An Introduction to the Bootstrap, Chapman & Hall/CRC Press, 49-54 pp., 1998.

695 Joyce, R. J., Janowiak, J. E., Arkin, P. A., and Xie, P. P.: CMORPH: A method that produces global precipitation estimates

696   from passive microwave and infrared data at high spatial and temporal resolution, J. Hydrometeorol., 5, 487-503,

697   10.1175/1525-7541(2004)005<0487:camtpg>2.0.co;2, 2004.

698 Joyce, R. J., and Xie, P.: Kalman Filter-Based CMORPH, J. Hydrometeorol., 12, 1547-1563, 10.1175/jhm-d-11-022.1, 2011.

699 Katsanos, D., Retalis, A., and Michaelides, S.: Validation of a high-resolution precipitation database (CHIRPS) over Cyprus
700  for a 30-year period, Atmospheric Research, 169, 459-464, doi:10.1016/j.atmosres.2015.05.015, 2016a.

701 Katsanos, D., Retalis, A., Tymvios, F., and Michaelides, S.: Analysis of precipitation extremes based on satellite (CHIRPS)
702  and in situ dataset over Cyprus, Natural Hazards, 83, 53-63, doi:10.1007/s11069-016-2335-8, 2016b.

703 Kummerow, C., Barnes, W., Kozu, T., Shiue, J., and Simpson, J.: The Tropical Rainfall Measuring Mission (TRMM) sensor
704  package, J. Atmos. Ocean. Technol., 15, 809-817, doi:10.1175/1520-0426(1998)015<0809:ttrmmt>2.0.co;2, 1998.

705 Long, D., and Singh, V. P.: Assessing the impact of end- member selection on the accuracy of satellite- based spatial variability
706  models for actual evapotranspiration estimation, Water Resources Research, 49, 2601-2618, doi:10.1002/wrcr.20208,
707  2013.

708 Lu, G. Y., and Wong, D. W.: An adaptive inverse-distance weighting spatial interpolation technique, Comput. Geosci., 34,
709  1044-1055, 10.1016/j.cageo.2007.07.010, 2008.

710 Maggioni, V., and Massari, C.: on the performance of satellite precipitation products in riverine flood modeling: A review,
711  Journal of Hydrology, 558, 214-224, 10.1016/j.jhydrol.2018.01.039, 2018.

712 Maggioni, V., Meyers, P. C., and Robinson, M. D.: A Review of Merged High-Resolution Satellite Precipitation Product
713  Accuracy during the Tropical Rainfall Measuring Mission (TRMM) Era, J. Hydrometeorol., 17, 1101-1117, 10.1175/jhm-
714  d-15-0190.1, 2016.

715 Mahmoud, M. T., Al-Zahrani, M. A., and Sharif, H. O.: Assessment of global precipitation measurement satellite products over
716  Saudi Arabia, Journal of Hydrology, 559, 1-12, 10.1016/j.jhydrol.2018.02.015, 2018.

717 Martens, B., Cabus, P., De Jongh, I., and Verhoest, N. E. C.: Merging weather radar observations with ground-based
718  measurements of rainfall using an adaptive multiquadric surface fitting algorithm, Journal of Hydrology, 500, 84-96,
719  doi:10.1016/j.jhydrol.2013.07.011, 2013.

720 Nash, J. E., Sutcliffe, J. V.: River flow forecasting through conceptual models, Part I - A discussion of principles, Journal of
721  Hydrology, 10, 282–290, doi.org/10.1016/0022-1694(70)90255-6, 1970.

722 Nogueira, S. M. C., Moreira, M. A., and Volpato, M. M. L.: Evaluating Precipitation Estimates from Eta, TRMM and CHRIPS
723  Data in the South-Southeast Region of Minas Gerais State-Brazil, Remote Sens., 10, 16, doi:10.3390/rs10020313, 2018.

724 Ning, S., Wang, J., Jin, J., and Ishidaira, H.: Assessment of the Latest GPM-Era High-Resolution Satellite Precipitation
725  Products by Comparison with Observation Gauge Data over the Chinese Mainland, Water, 8, 481-497,
726  doi:10.3390/w8110481,2016.

727 Paredes-Trejo, F. J., Barbosa, H. A., and Kumar, T. V. L.: Validating CHIRPS-based satellite precipitation estimates in
728  Northeast Brazil, J. Arid. Environ., 139, 26-40, doi:10.1016/j.jaridenv.2016.12.009, 2017.

729 Prakash, S.: Performance assessment of CHIRPS, MSWEP, SM2RAIN-CCI, and TMPA precipitation products across India,
730  Journal of Hydrology, 571, 50-59, 10.1016/j.jhydrol.2019.01.036, 2019.

731 Pessoa, F. C. L., Blanco, C. J. C., and Gomes, E. P.: Delineation of homogeneous regions for streamflow via fuzzy c-means in
732  the Amazon, Water Pract. Technol., 13, 210-218, doi:10.2166/wpt.2018.035, 2018.

733 Roy, T., Gupta, H. V., Serrat-Capdevila, A., and Valdes, J. B.: Using satellite-based evapotranspiration estimates to improve
734  the structure of a simple conceptual rainfall–runoff model, Hydrology and Earth System Sciences, 21, 879-896,
735  doi:10.5194/hess-21-879-2017, 2017.

736 Skofronick-Jackson, G., Petersen, W. A., Berg, W., Kidd, C., Stocker, E. F., Kirschbaum, D. B., Kakar, R., Braun, S. A.,
737  Huffman, G. J., Iguchi, T., Kirstetter, P. E., Kummerow, C., Meneghini, R., Oki, R., Olson, W. S., Takayabu, Y. N.,
738  Furukawa, K., and Wilheit, T.: The Global Precipitation Measurement (GPM) Mission for Science and Society, Bulletin
739  of the American Meteorological Society, 98, 1679-1695, 10.1175/bams-d-15-00306.1, 2017.

740 Shen, G. Y., Chen, N. C., Wang, W., and Chen, Z. Q.: High-resolution daily precipitation estimation data from WHU-SGCC

741 method: A novel approach for blending daily satellite (CHIRP) and precipitation observations over the Jinsha River Basin.

742 PANGAEA, https://doi.pangaea.de/10.1594/PANGAEA.900620, 2019.

743 Simanton, J. R., and Osborn, H. B.: RECIPROCAL-DISTANCE ESTIMATE OF POINT RAINFALL, Journal of the

744 Hydraulics Division-Asce, 106, 1242-1246, 1980.

745 Simpson, J., Adler, R. F., and North, G. R.: A PROPOSED TROPICAL RAINFALL MEASURING MISSION (TRMM)

746 SATELLITE, Bulletin of the American Meteorological Society, 69, 278-295, doi:10.1175/1520-

747 0477(1988)069<0278:aptrmm>2.0.co;2, 1988.

748 Sokol, Z.: The use of radar and gauge measurements to estimate areal precipitation for several Czech River basins, Stud.

749 Geophys. Geod., 47, 587-604, doi:10.1023/a:1024715702575, 2003.

750 Su, F. G., Gao, H. L., Huffman, G. J., and Lettenmaier, D. P.: Potential Utility of the Real-Time TMPA-RT Precipitation

751 Estimates in Streamflow Prediction, J. Hydrometeorol., 12, 444-455, doi:10.1175/2010jhm1353.1, 2011.

752 Thiemig, V., Rojas, R., Zambrano-Bigiarini, M., and De Roo, A.: Hydrological evaluation of satellite-based rainfall estimates

753 over the Volta and Baro-Akobo Basin, Journal of Hydrology, 499, 324-338, doi:10.1016/j.jhydrol.2013.07.012, 2013.

754 Trejo, F. J. P., Barbosa, H. A., Penaloza-Murillo, M. A., Moreno, M. A., and Farias, A.: Intercomparison of improved satellite

755 rainfall estimation with CHIRPS gridded product and rain gauge data over Venezuela, Atmosfera, 29, 323-342,

756 doi:10.20937/atm.2016.29.04.04, 2016.

757 Tung, Y. K.: POINT RAINFALL ESTIMATION FOR A MOUNTAINOUS REGION, J. Hydraul. Eng.-ASCE, 109, 1386-

758 1393, 10.1061/(asce)0733-9429(1983)109:10(1386), 1983.

759 Ushio, T., Sasashige, K., Kubota, T., Shige, S., Okamoto, K. i., Aonashi, K., Inoue, T., Takahashi, N., Iguchi, T., Kachi, M.,

760 Oki, R., Morimoto, T., and Kawasaki, Z.-I.: A Kalman Filter Approach to the Global Satellite Mapping of Precipitation

761 (GSMaP) from Combined Passive Microwave and Infrared Radiometric Data, Journal of the Meteorological Society of

762 Japan, 87A, 137-151, 10.2151/jmsj.87A.137, 2009.

763 Ushio, T., and Kachi, M.: Kalman filtering applications for global satellite mapping of precipitation (GSMaP), in: Satellite

764 rainfall applications for surface hydrology, Springer, 105-123, 2010.

765 Verdin, A., Rajagopalan, B., Kleiber, W., and Funk, C.: A Bayesian kriging approach for blending satellite and ground

766 precipitation observations, Water Resources Research, 51, 908-921, 2015.

767 Vila, D. A., de Goncalves, L. G. G., Toll, D. L., and Rozante, J. R.: Statistical Evaluation of Combined Daily Gauge

768 Observations and Rainfall Satellite Estimates over Continental South America, J. Hydrometeorol., 10, 533-543,

769 doi:10.1175/2008jhm1048.1, 2009.

770 Wang, P. H.: PATTERN-RECOGNITION WITH FUZZY OBJECTIVE FUNCTION ALGORITHMS - BEZDEK,JC, SIAM

771 Rev., 25, 442-442, 1983.

772 Xie, P., Joyce, R., Wu, S., Yoo, S.-H., Yarosh, Y., Sun, F., and Lin, R.: Reprocessed, Bias-Corrected CMORPH Global High-

773 Resolution Precipitation Estimates from 1998, J. Hydrometeorol., 18, 1617-1641, 10.1175/jhm-d-16-0168.1, 2017.

774 Xu, L., Chen, N., Zhang, X., Chen, Z., Hu, C., and Wang, C.: Improving the North American multi-model ensemble (NMME)

775 precipitation forecasts at local areas using wavelet and machine learning, Clim. Dyn., 53, 601-615, 10.1007/s00382-018-

776 04605-z, 2019.

777 Yang, T. T., Asanjan, A. A., Welles, E., Gao, X. G., Sorooshian, S., and Liu, X. M.: Developing reservoir monthly inflow

778 forecasts using artificial intelligence and climate phenomenon information, Water Resources Research, 53, 2786-2812,

779 doi:10.1002/2017wr020482, 2017.

780 Yang, Z., Hsu, K., Sorooshian, S., Xu, X., Braithwaite, D., and Verbist, K. M. J.: Bias adjustment of satellite-based precipitation

781 estimation using gauge observations: A case study in Chile, Journal of Geophysical Research: Atmospheres, 121, 3790-

782 3806, doi:10.1002/2015jd024540, 2016.

783 Yuan, Z., Xu, J. J., and Wang, Y. Q.: Projection of Future Extreme Precipitation and Flood Changes of the Jinsha River Basin

784   in China Based on CMIP5 Climate Models, Int. J. Environ. Res. Public Health, 15, 17, 10.3390/ijerph15112491, 2018.

785   Zambrano-Bigiarini, M., Nauditt, A., Birkel, C., Verbist, K., and Ribbe, L.: Temporal and spatial evaluation of satellite-based

786   rainfall estimates across the complex topographical and climatic gradients of Chile, Hydrology and Earth System Sciences,

787   21, 1295-1320, doi:10.5194/hess-21-1295-2017, 2017.

788   Zhang, X., and Chen, N. C.: Reconstruction of GF-1 Soil Moisture Observation Based on Satellite and In Situ Sensor

789   Collaboration Under Full Cloud Contamination, Ieee Transactions on Geoscience and Remote Sensing, 54, 5185-5202,

790   10.1109/tgrs.2016.2558109, 2016.

791   Zhang, Y. R., Sun, A., Sun, H. W., Gui, D. W., Xue, J., Liao, W. H., Yan, D., Zhao, N., and Zeng, X. F.: Error adjustment of

792   TMPA satellite precipitation estimates and assessment of their hydrological utility in the middle and upper Yangtze River

793   Basin, China, Atmospheric Research, 216, 52-64, 10.1016/j.atmosres.2018.09.021, 2019.